Surface conduction in *n*-type pyrite FeS_2 single crystals

Jeff Walter, Xin Zhang, Bryan Voigt, Ryan Hool, Mike Manno, Frazier Mork, Eray S. Aydil,* and Chris Leighton†
Department of Chemical Engineering and Materials Science, University of Minnesota, Minneapolis, Minnesota 55455, USA
(Received 30 July 2017; published 14 November 2017)

Pyrite FeS_2 has long been recognized as a high potential photovoltaic material, due to its exceptionally high optical absorption, low toxicity, and the abundance and low cost of its constituents. Despite the suitable band gap (0.95 eV), minority carrier diffusion length (100–1000 nm), and short-circuit current density, power conversion efficiencies in FeS_2-based solar cells have never exceeded 3% however, primarily due to low open circuit voltages ($V_{oc} \sim 0.1$ V). Surface phenomena have been implicated as the root cause of this low V_{oc}, recent experiments on *n*-type crystals providing evidence for surface conduction, including *p*-type surface inversion. Here we report a detailed study of electronic transport in a large set (∼120 samples) of thoroughly characterized vapor-transport-grown *n*-FeS_2 single crystals, with both as-prepared and mechanically polished surfaces. Abundant evidence for surface conduction is obtained from the temperature dependence of the resistance and its anisotropy, the thickness dependence of the resistivity, the sensitivity to surface preparation, and the nature of an observed surface insulator-metal transition. While the bulk transport is relatively reproducible, as-grown crystals display striking diversity in surface behavior, which is suppressed by polishing. Via detailed analyses, we demonstrate that the FeS_2 surface conduction is truly two dimensional, that it can influence in-plane transport even at room temperature, and that a *p*-type surface inversion layer can be unambiguously established, with no possibility of artifacts from hopping conduction. A nonlinear Hall effect is also observed, allowing us to constrain a two-channel conduction model we show capable of describing all field- and temperature-dependent transport data. Combined with simple arguments, these results place limits on the thickness of the surface conduction layer, which lie below ∼3 nm. Finally, in some crystals, for unknown reasons, the as-grown surface is definitively *n* type. These results highlight that while surface conduction is clearly important in pyrite FeS_2, and is gradually yielding to understanding, additional work is clearly warranted to further understand and control it.

DOI: 10.1103/PhysRevMaterials.1.065403

I. INTRODUCTION

Large-scale deployment of photovoltaic technology, with power generation capacity comparable to that of conventional fossil-fuel-based systems, is a revolutionary prospect. While ambitious, much progress towards this goal has now been made, as evidenced by regional grid parity of solar-to-electric power conversion technologies with existing power production methods [1]. This progress has been achieved primarily by improving efficiencies and lowering costs in conventional crystalline-Si (*c*-Si) solar cells, although thin film cells based on highly absorbing materials, such as CdTe and $CuIn_{1-x}Ga_xSe_2$ (CIGS), have also gained momentum [1]. While these second-generation thin film photovoltaic materials reduce materials costs, they also present disadvantages in terms of the use of rare (e.g., Cd, Te, In) and toxic (e.g., Cd, Te, Se) elements. This has led to a search for materials with the high absorption of CdTe and CIGS, but the abundance and low toxicity of *c*-Si [2]. One candidate in this regard is pyrite FeS_2, which not only has an outstanding visible absorption coefficient (e.g., $\alpha = 6 \times 10^5$ cm^{-1} at 1.9 eV) but is also comprised of abundant and nontoxic elements [2,3]. The electronic properties of pyrite FeS_2, which include a band gap $E_g = 0.95$ eV, minority carrier diffusion length of 100–1000 nm, and room temperature mobility μ up to 360 cm^{2}V^{-1}s^{-1}, are also encouraging [3].

Research on pyrite FeS_2 as a photovoltaic material thus has a significant history. FeS_2 started to garner interest in the mid-1980s, in fact, following the discovery of large quantum yields (>90% at 1.26 eV) and very large photocurrent densities in photoelectrochemical cells based on *n*-type FeS_2 single crystals [3–5]. While these values are impressive, they were accompanied by disappointingly low open circuit voltages ($V_{oc} < 0.2$ V), limiting solar-to-electric power conversion efficiencies to <2.8% [3]. Single crystal *n*-FeS_2/metal Schottky devices were also studied, resulting in large quantum yields (>70%) and short-circuit photocurrent densities (30 mA/cm^2), but again low V_{oc} (<0.1 V), resulting in power conversion efficiencies <1% [3,6]. Lastly, *p*-*i*-*n* type devices with polycrystalline FeS_2 thin films as the intrinsic (*i*) semiconductor were attempted, using electrolyte/FeS_2/TiO_2 structures [7]. The motivation here lies with the potential to use thin, highly absorptive *i* layers, minimizing the distance photoexcited carriers must diffuse to reach the *n*/*p* interfaces. Such structures resulted in quantum yields of only 10%, and efficiencies <1%, due to poor interfacial electron transfer [3,7].

One commonality uncovered in the above devices is the importance of FeS_2 surface preparation. The single crystal photoelectrochemical cells, for example, which yielded the record efficiency of 2.8%, only performed at this level when operated with a particular I^-/I^{3-} redox system, at a specific *p*H [3]. Similarly, the *n*-FeS_2 Schottky devices required an electrochemical proton reduction process at the FeS_2 single crystal surfaces prior to metal deposition to observe significant photoeffects and rectification [6]. The *p*-*i*-*n* devices discussed above also exhibited photocurrents and photovoltages heavily

*Corresponding author: aydil@umn.edu
†Corresponding author: leighton@umn.edu

dependent on the *p*H of the electrolyte solution, e.g., 0.35 V at $pH = 1$, increasing to 0.6 V at $pH = 12$ [7]. Based on this evidence for the importance of surface chemistry, a variety of surface characterization techniques were applied to *n*-FeS_2 crystals, such as low energy electron diffraction, x-ray and ultraviolet photoelectron spectroscopy, and low energy ion scattering [3]. Of particular interest, x-ray photoelectron spectroscopy revealed pinning of the Fermi level near the valence band edge at the FeS_2 surface [8,9]. Surface electronic states resulting from the lowered symmetry of surface Fe ions (from octahedral to square pyramidal) were proposed as an explanation for this Fermi level pinning, and the subsequent 0.65 eV band bending required to accommodate it [3,8,9]. These surface states were suggested to reside in the gap, above the valence band maximum, potentially accounting for the low photovoltages and high photocurrents of *n*-FeS_2/metal junctions via the creation of leaky tunnel barriers [3,8,9]. In light of these findings, and in the absence of an immediate solution, photovoltaic research on FeS_2 dwindled.

Following a 2009 study on the economic viability of various photovoltaic material candidates, where FeS_2 was an obvious standout due to the high elemental abundance and low cost of Fe and S [2], research on FeS_2 experienced a substantial revival. While a few recent studies have characterized FeS_2 photovoltaic devices, confirming their relatively poor performance [10–15], most have focused on fundamental challenges with pyrite. These include: (i) Synthesis of high quality, phase-pure, stoichiometric FeS_2 crystals and films, (ii) understanding and controlling doping in FeS_2, and (iii) understanding the surface phenomena that have plagued FeS_2 devices. Considering phase purity and stoichiometry first, note that non-negligible phase fractions of the marcasite FeS_2 polymorph, or nonsemiconducting phases such as pyrrhotite $Fe_{1-\delta}S$, have long been cited as potential causes for poor solar cell performance in pyrite [3,16,17]. However, a growing number of recent studies have claimed rigorously phase-pure near-stoichiometric pyrite FeS_2 crystals and films by combining an array of characterization techniques, including laboratory x-ray diffraction [10,11,13–15,18–26], synchrotron x-ray diffraction [18,19,27], energy dispersive spectroscopy [20,23,25,28], Raman spectroscopy [10,11,13–15,18,20,23,25–28], x-ray photoelectron spectroscopy [18–20,28], and magnetometry [15,18,20,23,25]. The latter is particularly powerful due to the presence of magnetic order in all Fe-S compounds other than diamagnetic FeS_2 [20,23]. A consensus is thus emerging that while phase purity and homogeneity are concerns in pyrite, they are likely not the fundamental origin of poor FeS_2 solar cell performance.

The issue of understanding and controlling doping in FeS_2 has yielded fewer advances, although some progress has been made. Recent work of our own, for example, has provided a potential resolution to the "doping puzzle" in pyrite, i.e., the observation that unintentionally doped single crystals are generally found to be *n* type, whereas unintentionally doped thin films are typically *p* type [25]. That work involved a broad study of a large set of FeS_2 crystals and films, and concluded, contrary to common belief, that high μ films can certainly be *n* type, much like single crystals. As μ decreases, an *apparent* crossover from *n* to *p* type was observed, based on both Hall effect and thermopower measurements. This was found to correlate with a crossover from diffusive to hopping transport, however, which is known to artificially invert the sign of Hall and Seebeck coefficients [20,23,25,29–35]. It was thus concluded that the widely observed *p*-type behavior in unintentionally doped low-μ FeS_2 films can easily arise as an artifact of hopping, providing a potential resolution to the doping puzzle [25]. Many open issues remain, however, including the true origin of the *n* doping in unintentionally doped crystals and films, the occasional reports of high μ *p*-type films (which cannot be explained by hopping) [10,36–39], and the frequently encountered heavy doping and low μ in pyrite thin films [13,18,19,23,25]. Of most relevance to the current work, while S vacancies (V_S) provide a viable explanation for *n* doping [3,14,27], additional work to gather stronger evidence is clearly needed.

In terms of understanding surface phenomena in FeS_2, substantial recent progress has been made by utilizing high quality single crystals as model systems. Scanning tunneling spectroscopy measurements on FeS_2(001), for example, suggest that the surface band gap can be as small as 0.4 eV, substantially below the accepted bulk value of 0.95 eV, potentially dropping the maximum photovoltage to <0.4 eV [40]. This surface gap lowering has also been evidenced from density functional calculations, where E_g was found to be a function of stoichiometry [41,42]. Low density states resulting in an ill-defined conduction band onset are an issue even in bulk pyrite, in fact [43,44]; this general area of research clearly warrants further work. Recently, the impact of surface phenomena on bulk electronic transport was also reported [27]. In an important advance, Limpinsel *et al.* observed surface-dominated conduction at low temperature (T) in polished flux-grown FeS_2 single crystals, after freeze-out of the bulk *n*-type carriers [27]. This conclusion was supported not only by the unusual T dependence of the resistivity, but also by thickness scaling and surface treatment studies. Consistent with the x-ray photoelectron spectroscopy findings discussed above [8], Limpinsel *et al.* went on to conclude that the surface Fermi level becomes pinned near the valence band maximum in FeS_2 single crystals, resulting in a *p*-type surface conductive layer, potentially explaining the low V_{oc} in pyrite solar cells [27]. While the evidence for surface conduction presented is strong, some uncertainty nevertheless remains over whether the surface layer is definitively *p* type. Specifically, the primary evidence for a *p*-type inversion layer in Limpinsel *et al.* derives from suppression of the Hall coefficient at low T, where surface conduction dominates. Although this can be captured by a two-channel conduction model with an inverted (i.e., *p*-type) surface, the Hall coefficient itself did not clearly invert, instead fluctuating between small positive and negative values at low T. Further complicating matters, the surface layers in that work were quite resistive, making it difficult to rule out artificial inversion of the Hall coefficient due to the onset of Efros-Shklovskii variable range hopping [20,23,25,29–32].

Another recent study of *n*-type FeS_2 single crystals by Caban-Acevedo *et al.* provided additional important information [14]. That work combined T-dependent resistivity measurements with optical spectroscopy and photoelectrochemical studies, characterizing defect-related behavior in both the bulk and surface of chemical vapor transport (CVT)-grown crystals. Pinning of the surface Fermi level near the valence band edge

was again concluded, along with a high density of unknown surface acceptors, although it was argued that this alone does *not* satisfactorily explain the low pyrite V_{oc}. The authors in fact proposed that this situation should *increase* V_{oc}, via the creation of a buried p-n junction. Instead, a high density of deep donor states in the bulk were implicated as the source of the low V_{oc}. Additionally, a clear change in character of the resistivity and Hall coefficient was found at low T, not dissimilar to that seen by Limpinsel *et al.*, but was taken not as evidence of surface conduction or surface inversion, but rather as evidence for the onset of Mott variable range hopping among bulk deep donors [14].

While these recent studies on high quality n-type bulk single crystals of FeS_2 thus advance the state of knowledge in the field, there remain open issues. First, it is clearly desirable to further document and confirm surface conduction in pyrite crystals, ideally also answering questions about the *nature* of that conduction. In what part of the phase space is such surface conduction with respect to the insulator-metal transition, for instance? What are the doping levels and mobilities, and is the conduction metallic, diffusive, or hopping-based? Related to this, can surface inversion be more definitively established, and can the thickness of the surface layer be accurately determined? The reproducibility and universality of such phenomena should also be addressed, particularly with regard to different synthesis methods and surface preparations. Ultimately, with sufficient understanding of surface conduction in pyrite FeS_2 one could then hopefully conclude whether it is intrinsic, whether it results from surface states or some other defect, and thus how such behavior might be controlled and mitigated. An important point in this regard, which has not been extensively discussed, is that anomalous surface transport effects have also been documented in other pyrite-structure transition metal disulfides, raising the possibility that they are generic to this materials class. Metallic surface conduction in the antiferromagnetic Mott insulator NiS_2 has been observed, for example, accompanied by weak ferromagnetism that is also perturbed by the surface [45,46]. In the metallic ferromagnets CoS_2 and $Co_{1-x}Fe_xS_2$, important surface effects have also been uncovered, including a minority spin surface state reducing the Fermi level spin polarization in what are otherwise half-metallic candidates [47]. We add parenthetically that the current emphasis in the condensed matter physics community on topological insulators adds a further layer of interest in this context, due to the high interest in the characterization of metallic surface states on insulating single crystals [48–51].

Motivated by the above issues, we present here a detailed electronic transport study of a large set of high quality, phase-pure, thoroughly characterized, unintentionally doped n-type pyrite FeS_2 single crystals. We first confirm surface conduction, which we find to be clearly reflected in the T dependence of the resistance and its in-plane anisotropy, the thickness dependence of the resistivity, and the strong sensitivity to surface preparation. As-grown (untreated) surfaces display striking variability in transport, in fact, which is suppressed by mechanical polishing. Notably, a low T insulator-metal transition (IMT) taking place in such crystals is found to occur close to the quantum resistance $h/e^2 = 26\,\mathrm{k}\Omega$, a simple demonstration that the conduction is not only surface dominated but also truly two dimensional (2D). Studying surfaces on both sides of the IMT, simple analyses based on the temperature and field dependence of the resistance in the weakly localized and hopping regimes are then used to place upper limits on the thickness of the surface conduction layer, which we find to lie at ∼3 nm. Detailed Hall effect measurements are also presented, providing direct proof of a transition from n-type bulk to p-type (i.e., inverted) surface conduction on cooling. This occurs even in crystals where hopping conduction can be definitively ruled out, eliminating the possibility of artifacts. The nonlinear Hall effect that is expected at an $n \rightarrow p$ crossover is also observed, and is shown to significantly constrain a two-channel conduction model capable of describing all field- and temperature-dependent data for all crystals. Poorly understood observations nevertheless remain, including n-type surface conduction in some crystals, and the aforementioned diversity in as-prepared surface electronic properties. These point to uncontrolled surface factors in FeS_2, and the clear need for additional research.

II. EXPERIMENTAL METHODS

Bulk pyrite FeS_2 single crystals were grown via CVT, as described previously [20,25]. Briefly, crystals were synthesized in an evacuated (10^{-6} Torr) quartz tube placed in a two-zone tube furnace, with FeS_2 powder (Alfa Aesar, 99.9% purity) and S (CERAC, 99.999% purity) as the source materials, and $FeBr_2$ (Sigma-Aldrich, 99.999% purity) as the transport agent. After an initial 3 day period with an inverted temperature gradient to "clean" the growth zone, temperatures in the precursor and growth zones were set at 670 and 590 °C, respectively, for ∼3 weeks. Only organic solvents (acetone, methanol, isopropanol) were used to clean the crystals of S and $FeBr_2$ residue post-growth; no other surface chemical treatments were employed.

Powder x-ray diffraction (XRD) was performed using Cu K_α (1.5418 Å) radiation on a Bruker-AXS D5005 system, and high resolution single crystal XRD was performed on a Panalytical X'Pert Pro system using monochromated Cu $K_{\alpha,1}$ (1.5406 Å) radiation. Contact mode atomic force microscopy (AFM) was done in a Bruker Nanoscope V Multimode 8 system. Raman spectra were collected in the backscattering geometry, using a WiTec alpha300R confocal microscope equipped with a UHTS 300 spectrometer and a DV401 CCD detector. Chemical composition and purity were assessed via energy dispersive x-ray spectroscopy (EDX) and particle-induced x-ray emission spectroscopy (PIXE). EDX was performed in a JEOL 6500F field emission scanning electron microscope with a Thermo-Noran Vantage EDX system, analysis using Thermo-Noran's System Six EDX software package providing elemental composition to a detection limit ∼1%. PIXE was performed in a National Electrostatics Corporation (NEC) MAS 1700 pelletron tandem ion accelerator with a 4000 keV He^{2+} ion beam, where x-ray detection was achieved with a Kevex Si drift detector (Model 3700 with a 5 μm thick Be window) coupled with a 25 μm thick Al filter. PIXE data analysis was performed using the software package GUPIX [52], providing composition determination to a trace metal detection limit of 10−100 ppm, dependent on the element.

Crystals were prepared for electrical transport measurements by identifying a large {111} facet and polishing from the opposite (back) side to form a parallelepiped. The polishing procedure consisted of grinding using SiC paper of progressively finer grit (down to 1200 grit), followed by polishing with a 3 μm diamond slurry, resulting in a backside RMS surface roughness <5 nm over 10-μm-scale areas. Contacts were then placed in a van der Pauw geometry [53] on unpolished {111} facets on the top surface using sputter-deposited metals (Mg, Co, Ni, Au, or Pt) with Au overlayers, or soldered In. Attention was paid to ensure the contact behavior was Ohmic and free of self-heating at all T. Four terminal resistance measurements were made dc using a Keithley 220 current source and Keithley 2002 voltmeter, or ac using a Lakeshore 370 ac resistance bridge at 13.7 Hz, depending on the magnitude of the resistance. Such measurements were performed in cryostats equipped with 9 T superconducting magnets, from 1.5 to 300 K. These significant magnetic fields and optimized temperature stability ($\pm$10 mK) prove crucial for the Hall effect and magnetoresistance measurements presented below. Finally, for a subset of samples the top surface was also polished to provide a comparison to as-grown surfaces. This was done by polishing a pristine facet using the same procedure noted above, i.e., grinding with SiC paper before polishing with a 3 μm diamond slurry to a roughness <5 nm.

III. RESULTS

A. Structural and chemical characterization

The products of the CVT growth consisted of void-free, {111}-faceted FeS_2 crystals with dimensions up to 5 mm [see Fig. 1(a), inset], with typical growth rates of ~1.5 mg/day. Phase purity of powdered crystals was confirmed by laboratory XRD, as shown in Fig. 1(a). All peaks can be indexed to the reference pattern for cubic pyrite FeS_2 [PDF 00-042-1340, Fig. 1(b)], the extracted lattice parameter of 5.418 $\pm$ 0.001 Å matching very well the accepted value of 5.418 Å [3,14,27]. As shown in the inset to Fig. 1(a) for a representative {111}-faceted sample, the crystals exhibit mirrorlike surfaces. The AFM height image in the inset of Fig. 1(b) in fact indicates atomic-level roughness on a 1−10 μm lateral scale, the step height of the terraces, 3.2 $\pm$ 0.4 Å, being consistent with the (111) interplanar spacing of 3.13 Å for pyrite FeS_2. This CVT method thus produces as-grown surfaces that are substantially smoother than some other crystal growth approaches. Figure 1(c) shows the wide-angle XRD from a typical triangular facet on a representative crystal, in which only 111 and 222 peaks appear, as expected. The rocking curve through the 111 peak [inset to Fig. 1(c)] reveals a full-width at half-maximum (FWHM) of only 0.008° (the instrumental broadening is 0.002°), confirming low mosaic spread, and thus low overall defect density. Additional evidence of phase purity is provided by the Raman spectrum from a representative {111} single crystal facet shown in Fig. 2(a). This spectrum exhibits sharp peaks corresponding to the S_2 libration (342 cm^{-1}), in-phase stretch (378 cm^{-1}), and coupled libration/stretch (430 cm^{-1}) modes, characteristic of pyrite FeS_2 [54].

Moving to characterization of chemical composition, excluding the usual C and O signals due to surface contamination,

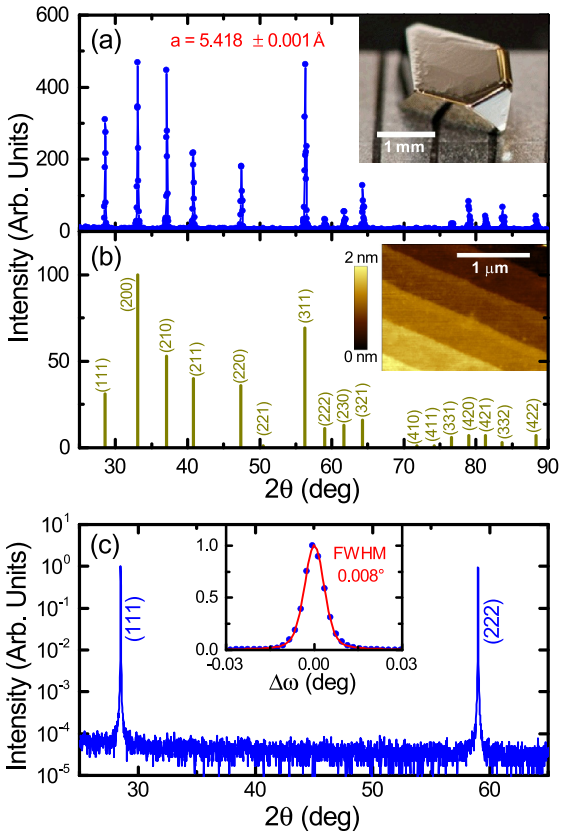

FIG. 1. Structural characterization of FeS_2 single crystals. (a) Wide angle x-ray diffraction from a representative powdered FeS_2 single crystal, with the reference pyrite FeS_2 pattern (PDF 00-042-1340) shown in (b); the extracted lattice parameter is shown. A photograph of a typical crystal is shown in the inset to (a), and a contact mode atomic force microscopy height image is shown in the inset to (b). (c) Wide angle x-ray diffraction from the 111 facet of a single crystal. The inset to (c) shows a rocking curve (transverse scan) through the 111 peak, with a pseudo-Voigt fit (solid red line) giving a full-width at half-maximum of 0.008°.

only Fe and S core transitions are observed in the EDX spectrum from a representative {111} FeS_2 crystal facet shown in Fig. 2(b). The extracted S:Fe ratio is 1.98 $\pm$ 0.1 (dominated by systematic error), indicating stoichiometric FeS_2 within the accuracy of the EDX instrument used; no impurities were found above the ~1% EDX detection limit. PIXE measurements were also performed, which, due to the elimination of Bremsstrahlung, provide a greatly improved trace metal detection limit of 10–100 ppm. The PIXE spectrum from a {111} facet of a representative FeS_2 crystal is shown in Fig. 2(c), exhibiting the expected core transitions of Fe and S (green and yellow dashed lines, respectively), Fe escape and sum peaks (labeled), as well as detector artifact peaks (also labeled). Of note, however, is the presence of a small shoulder at 7.47 keV (red dashed line), which we assign to Ni. For the particular crystal in Fig. 2(c), analysis using GUPIX indicates a Ni concentration of 140 $\pm$ 25 ppm, with a detection limit (based on the background intensity around 7.47 keV) of 80 ppm. This concentration varies from crystal to crystal [even in nominally identical (e.g., same growth tube)

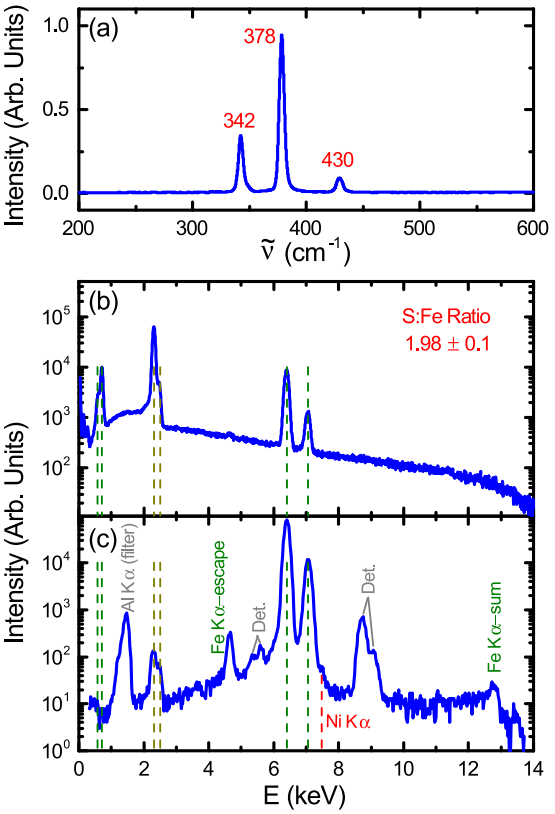

FIG. 2. Chemical characterization of FeS_2 single crystals. (a) Raman spectrum with the peak positions labeled. (b) Energy dispersive x-ray spectrum with Fe and S core transitions marked by green and yellow dotted lines, respectively, and the calculated S:Fe ratio shown. (c) Particle induced x-ray emission spectrum with Fe, S, and Ni core transitions marked by green, yellow, and red dotted lines, respectively. Detector artifact peaks are labeled in gray, and a weak Ni signal is labeled red.

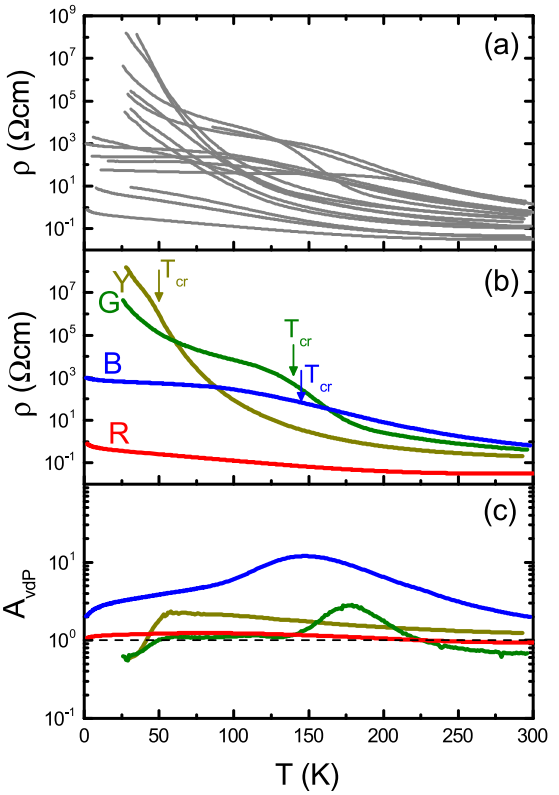

FIG. 3. Diversity in electronic transport properties in as-grown FeS_2 crystals. (a) Temperature dependence of the resistivity ρ for 16 FeS_2 crystals. (b) Temperature dependence of ρ for four representative samples from the larger set shown in (a). These are labeled "sample B" (blue), "sample Y" (dark yellow), "sample R" (red), and "sample G" (green). (c) Temperature dependence of the van der Pauw anisotropy A_{vdP} for the representative samples shown in (b), with the same color code. In (b) the crossover temperatures marked by T_{cr} are the points at which two-channel modeling indicates equal (50%) current flow through the bulk and surface.

crystals], from 40–300 ppm, with an average detection limit of ∼50 ppm. These Ni impurities derive from the commercial FeS_2 precursor powder used in the CVT growth, which has ∼ 500 ppm Ni according to the manufacturer's impurity analysis [55]. The potential role of the $O(100$ ppm) Ni impurities in these crystals is returned to below. No other impurities were observed by PIXE, including Br (with a detection limit of 100 ppm), which could potentially incorporate from the $FeBr_2$ transport agent during growth. Note that the sampling depth in FeS_2 under these PIXE conditions is ∼10 μm, limited by the penetration depth of the incident He^{2+} ions.

B. Electronic transport: Evidence for surface conduction

The T dependence of the resistivity (ρ) for 16 representative unintentionally doped FeS_2 single crystals is summarized in Fig. 3(a). The first, and most striking observation, is that while the 300 K resistivity values of these nominally identical as-grown crystals are relatively tightly clustered, the low T behavior is remarkably diverse. $d\rho/dT$ is generally negative (i.e., semiconductinglike) but the resistivity at 30 K, for example, varies by over eight orders of magnitude. A second notable feature from Fig. 3(a) is the unusual form of $\rho(T)$ seen in many crystals, where an inflection point occurs between ∼100 and 200 K. This behavior is illustrated more clearly in Fig. 3(b), where the $\rho(T)$ of four particular crystals, labeled "B" (blue), "Y" (yellow), "G" (green), and "R" (red), are highlighted. These four crystals represent the full spectrum of qualitative behaviors in this study, and are highlighted throughout this paper. Note that none of these four are unique, each being representative of a class of behavior found in multiple as-grown crystals.

The $\rho(T)$ of sample G is qualitatively similar to that reported in the recent publications discussed in the Introduction [27]. Typical semiconducting behavior occurs down to ∼150 K, at which point abrupt flattening of $\rho(T)$ is found, immediately suggestive of a crossover between two conduction regimes. This was shown by Limpinsel *et al.* to arise due to a crossover from bulk-dominated to (more conductive) surface-dominated transport in polished flux-grown FeS_2 crystals, after freeze-out of the semiconducting interior on cooling [27]. As illustrated in Fig. 3(b) we label this inflection point T_{cr}. Sample Y represents a slightly different behavior from G in that T_{cr} is significantly lower (∼50 K), demonstrating that the conduction mechanism crossover can occur over widely varying temperatures in these as-grown crystals. Yet

different behavior is exemplified by sample B, which, despite similar T_{cr} to sample G, has much lower resistivity at low T, with correspondingly weaker $\rho(T)$. This demonstrates that substantial variability can also occur in the $\rho(T)$ behavior in the low T conduction regime of these FeS_2 crystals. Finally, sample R is representative of a number of crystals in this study that not only exhibit no clear inflection in $\rho(T)$ between 1.5 and 300 K, but also have much lower overall resistivity, with a very weak T dependence. Thus, while the 300 K resistivity of these as-prepared unintentionally doped FeS_2 crystals varies relatively little from crystal-to-crystal, the low temperature resistivity, low temperature $\rho(T)$, and T_{cr}, all vary substantially.

Further evidence that T_{cr} indeed marks a crossover between two distinct conduction channels is provided in Fig. 3(c). Plotted here is the T dependence of the in-plane resistance anisotropy ratio A_{vdP}. This is obtained from the two orthogonal resistance (R) values measured in the van der Pauw configuration [53] on these parallelepiped crystals, as in the Montgomery method used for characterizing anisotropic conductors [56]. Figure 3(c) shows that clear correlations exist between $A_{vdP}(T)$ and $\rho(T)$, broad peaks in A_{vdP} always preceding the inflection in $\rho(T)$ on cooling. In sample G, for instance, a peak in A_{vdP} develops around 175 K, followed by T_{cr} at 140 K. Similarly, in samples Y and B broad peaks in A_{vdP} occur around 60 and 150 K, respectively, where the T_{cr} values are 50 and 145 K. While the shape of $A_{vdP}(T)$ varies substantially from crystal-to-crystal, the overall qualitative behavior is consistent, with small resistance anisotropy occurring in the low and high T limits, and an intermediate temperature peak preceding T_{cr}. In a similar vein, sample R, consistent with Fig. 3(b) where no inflection is seen, exhibits negligible resistance anisotropy at all T, with no peak in A_{vdP}. Quite simply, we interpret these peaks in $A_{vdP}(T)$ at just above T_{cr}, which have not been previously reported, as an indication of inhomogeneous current flow at the crossover between the two conduction channels.

As in the work of Limpinsel *et al.* [27], thickness scaling was pursued as a simple means to test whether the two conduction channels deduced from $\rho(T)$ and $A_{vdP}(T)$ can be simply ascribed to the bulk and surface. This was achieved by repeating $\rho(T)$ measurements after progressive polishing of crystals from the backside (i.e., preserving the as-grown top surface), as shown in Fig. 4(a) for samples B, G, and R. Initial thicknesses were 980–1250 μm, reduced in steps to ~100 μm by backside polishing. The results categorically confirm a transition from bulk-dominated to surface-dominated conduction. Considering samples G and B, for example, the deduced ρ values are essentially independent of thickness at 300 K, consistent with uniform conduction through the depth of the crystal. As T_{cr} is approached on cooling, however, both crystals begin to exhibit a deduced ρ that decreases approximately linearly with decreasing thickness (see Supplemental Material Fig. S1 [57]), indicating a nonuniform conduction profile, specifically a surface region more conductive than the bulk. This is consistent with the conclusions of Limpinsel *et al.* [27]: A more conductive surface region shunts the current at low T, after freeze-out of the semiconducting interior, leading to a transition at T_{cr} from bulk-dominated to surface-dominated conduction in these in-plane measurements. Unsurprisingly, at

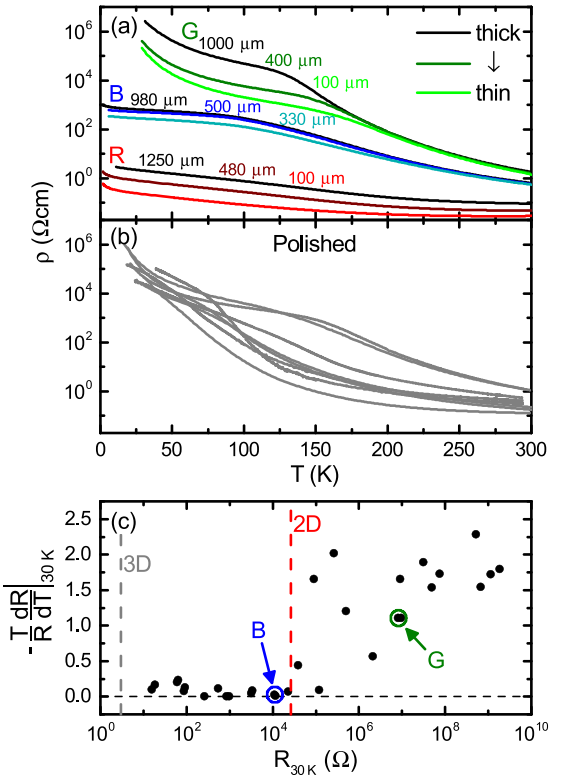

FIG. 4. Evidence for surface conduction in FeS_2 crystals. (a) Temperature and thickness dependence of the resistivity ρ for three representative as-grown crystals. The thicknesses are labeled and color coded in green, blue, and red for samples G, B, and R, respectively. (b) Temperature dependence of ρ for eight polished FeS_2 crystals. (c) The negative dimensionless temperature coefficient of resistance evaluated at 30 K $[-(T/R)(dR/dT)]$ vs the 30 K sheet resistance R_{30K} for all crystals measured in this work. The 2D quantum resistance $h/e^2 \approx 26\,k\Omega$ (i.e., the inverse of the 2D minimum metallic conductance) is marked by the red dotted line, the inverse 3D minimum metallic conductivity (for a 0.1-mm-thick crystal) being marked by the gray dotted line.

temperatures within the crossover region between bulk- and surface-dominated conduction the current flow is inhomogeneous, leading to the resistance anisotropy shown in Fig. 3(c). We emphasize here that the resistivity values below T_{cr} in Figs. 3 and 4 are thus *apparent* values, the true resistivity requiring knowledge of the surface conduction layer thickness (as returned to below). Another important point is that while the conduction at 300 K in samples such as B and G is not dominated by the surface in these *in-plane* measurements, in the vertical geometry relevant to solar devices this surface region always affects conduction, even at 300 K, as the bulk and surface conduction channels appear in series. Within this simple picture, the behavior of sample R [Fig. 4(a)] is of particular interest, due to the clear thickness dependence of ρ at 300 K. This new observation indicates that even in an in-plane geometry as-prepared FeS_2 crystals can exhibit surface-influenced conduction at 300 K.

The substantial role played by surface treatment in the electronic transport properties of FeS_2 crystals, in itself additional evidence for surface conduction, is emphasized

in Fig. 4(b). Shown here is the $\rho(T)$ behavior of eight single crystals not with as-prepared top surfaces, but rather top surfaces that have been mechanically polished via the procedure discussed in Sec. II. The striking observation from these data is the dramatic decrease in the diversity of the surface conduction after polishing. The 8 order of magnitude variation in 30 K resistivity in Fig. 3(a) (for untreated top surfaces) is suppressed to only 2 orders of magnitude in Fig. 4(b), although the crossover from bulk- to surface-dominated transport is maintained. The latter is evident from the inflection present in $\rho(T)$ [Fig. 4(b)], in addition to the peaks occurring in $A_{\mathrm{vdP}}(T)$ and the characteristic thickness scaling (data not shown). The apparent low T (i.e., surface dominated) ρ values cluster in the $10^5-10^6\ \Omega$ cm range, similar to sample G, the behaviors such as those represented by as-prepared samples B and R being completely eradicated. These results are in fact in good agreement with the recent reports of Limpinsel *et al.* [27] on mechanically polished flux-grown crystals, both in terms of the absolute low T resistivity values and the qualitative form of $\rho(T)$. The diversity in surface conduction observed in as-prepared crystals (Fig. 3) is thus strongly suppressed after mechanical polishing to a top surface roughness of $\sim$5 nm. Consistent with this, no correlations were uncovered in this work between the surface (i.e., low T) resistance and the Ni impurity concentration from PIXE. Variation in Ni impurity concentration is thus not the origin of the diversity in surface conduction behavior observed here. In particular, crystals such as sample R do not have unusually high or low Ni concentration.

We note at this stage that while the apparent reproducibility and repeatability of transport results on mechanically polished crystals is noteworthy, as-grown surfaces nevertheless provide important advantages for fundamental study. One set of such will become apparent below (Sec. III C), when the diversity in surface resistance and $R(T)$ behavior is used to draw important conclusions on the nature of the surface conduction. Similarly, crystals with more conductive surfaces, such as sample B, will be used below to definitively establish a p-type surface inversion layer, with no possibility of hopping artifacts. In addition to these points, as-grown surfaces, while yielding diverse surface electronic properties, nevertheless present very low surface roughness [consider Fig. 1(b), inset], much lower than polished ones. In fact, prior estimates of the thickness of the surface conductive layer in FeS_2 crystals lie in the 0.7–4.4 nm range [14,27,41], comparable to or even less than the roughness of polished surfaces (1–10 nm), raising obvious concerns. For the remainder of this paper, with the goal of understanding the native surface transport properties of pyrite, we thus focus on crystals with as-grown (unpolished) top surfaces.

C. Electronic transport: Nature of surface conduction

One powerful illustration of the utility of studying the diverse surface transport behavior found in as-prepared crystals is provided in Fig. 4(c). This figure plots the low T (30 K) dimensionless temperature coefficient of resistance $-\frac{T}{R}\frac{dR}{dT}|_{30\ \mathrm{K}}$ as a function of the low T sheet resistance $R_{30\mathrm{K}}$ for multiple crystals. The motivation for such a plot is to examine in more detail the apparent correlation between the low T value of dR/dT and the absolute value of R suggested by Figs. 3(a) and 3(b) and Figs. 4(a) and 4(b). As shown in Fig. 4(c) this correlation is indeed strong, the dimensionless temperature coefficient of resistance decreasing with decreasing R, eventually approaching zero. This is, of course, nothing other than the behavior expected at any IMT, where R is expected to become essentially T independent at the critical point [58,59]. What is unusual in Fig. 4(c), however, is the absolute value of R at which $dR/dT \rightarrow 0$. As shown by the vertical dashed red line this occurs precisely at the quantum resistance $h/e^2 = 26\,\mathrm{k}\Omega$, which is the expectation for a *two-dimensional* IMT [58,59]. For comparison, the vertical gray dashed line in Fig. 4(c) shows the expectation for a three-dimensional IMT, calculated from the Mott minimum metallic conductivity ($\sigma_{\mathrm{min}} = \frac{0.026e^2}{\hbar a_{\mathrm{B}}}$) for a uniformly conductive 0.1-mm-thick FeS_2 crystal (a_{B} here is the donor Bohr radius, calculated from the dielectric constant and electron effective mass) [58,59]. Figure 4(c) thus graphically illustrates that the low T conduction in these FeS_2 crystals is not only surface dominated, but in fact truly 2D in nature. Qualitatively, crystals such as sample B in Figs. 3(b) and 4(a) illustrate this point, having essentially flat $\rho(T)$ at low T (i.e., dR/dT approaching zero) at unphysically large apparent ρ values for a 3D conductor ($\sim 10^3\ \Omega$cm). These correspond to R values of $\sim$10 kΩ, however [see Fig. 4(c), where sample B is indicated with the blue arrow], below h/e^2, where a 2D conductor would be expected to have negligible dR/dT. Related to a comment in the Introduction, this observation of essentially flat $\rho(T)$ at anomalously high apparent ρ values provides a clear parallel with the surface conduction phenomena seen in topological insulator systems [48–51].

Detailed analyses of the T and B (magnetic flux density) dependence of the resistance in samples on either side of the IMT illustrated in Fig. 4(c) provide much additional insight into the surface conduction in these as-grown FeS_2 crystals. We focus for this purpose on samples B and G, which are highlighted by arrows in Fig. 4(c). While these samples have similar T_{cr}, crystal B exhibits surface conduction close to the 2D IMT, while G exhibits surface conduction deep on the insulating side. We note again here that the latter is quite similar to the polished surfaces studied by Limpinsel *et al.* [27]. We first discuss the magnetoresistance (MR), which is plotted in Fig. 5(a) as a function of T for both samples. The magnetic field here is applied perpendicular to the crystal plane, with a fixed value $B_\perp = 9$T. Above $\sim$175 K the two samples exhibit near-identical behavior, the positive MR increasing on cooling, reaching 4%–5% at 175 K. As shown in the inset to Fig. 5(a) at a representative T of 270 K, this MR is parabolic with $B_\perp$, having all the features associated with the ordinary MR effect one would typically anticipate in a nonmagnetic semiconductor with diffusive transport [60]. Cooling below T_{cr}, however [$\sim$150 K in these cases, see Fig. 3(b)], induces qualitatively different MR(T) in the two samples; sample B crosses over to a negative MR at low T, where the surface dominates, whereas sample G maintains a positive MR that grows on cooling.

Starting with sample B, the additional analysis of $R(T, B_\perp)$ provided in Figs. 5(b) and 5(c) provides direct insight into the origin of the negative MR at low T. Figure 5(b) first focuses on the functional form of $R(T)$ at the lowest measured T

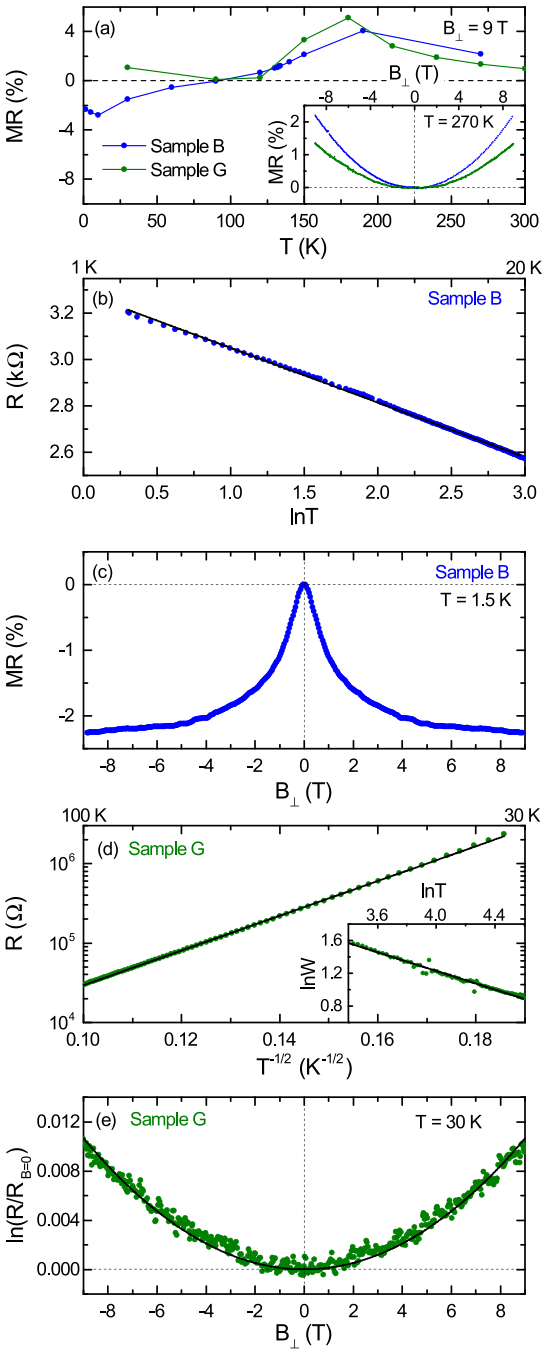

FIG. 5. Nature of the FeS_2 surface conduction. (a) Temperature dependence of the magnetoresistance (MR) at magnetic field $B_\perp = 9$ T for samples B and G in blue and green, respectively. The solid lines are guides to the eye. The inset shows the $B_\perp$ dependence of the MR at 270 K for samples B and G. (b) Resistance (R) vs ln T for sample B, from 1.5 to 20 K, with a straight line fit shown in black. (c) $B_\perp$ dependence of the sample B MR at 1.5 K. (d) Resistance R for sample G vs $T^{-1/2}$, from 30 to 100 K, with a straight line fit in black. The inset shows a Zabrodskii plot (ln W vs ln T, where $W = -d\ln R/d\ln T$) for the same temperature range, with a straight line fit. The fit yields the parameters $m = 0.57$ and $T_0 = 1298$ K. (e) $B_\perp$ dependence of the sample G logarithmic magnetoresistance ratio [$\ln(R/R_{B=0})$] at 30 K, and the resulting fit (black solid line) to an Efros-Shklovskii variable range hopping model, yielding a localization length $L_c = 3.4$ nm.

(1.5–20 K), which is found to be logarithmic. This is the expected form for weakly localized conduction in 2D, where both the weak localization and electron-electron interaction corrections to the conductance are logarithmic in T:

$$G(T) = G_0 + \frac{e^2}{2\hbar\pi^2}\left[p + \left(1 - \frac{3}{4}\widetilde{F_\sigma}\right)\right]\ln\left(\frac{T}{T_0}\right). \quad (1)$$

Here, G_0 and T_0 are constants, p is the exponent defining the power law T dependence of the inelastic scattering time, and $\widetilde{F_\sigma}$ is the conductivity Fermi liquid interaction parameter [61]. Equation (1) is in fact in reasonable quantitative agreement with our data, as determined by ignoring the electron-electron interaction term in (1) (i.e., assuming weak localization is dominant), which yields a fitted $p = 1.7$, a reasonable value [61]. The negative MR occurring in perpendicular fields at low T in this sample [Fig. 5(a)] is then expected, arising due to the field-induced decoherence of destructively interfering transport paths, characteristic of weak localization [58,59,61,62]. The field dependence of this MR at 1.5 K is shown in Fig. 5(c), indeed displaying the qualitative characteristics of the negative MR associated with weak localization. The MR is apparent at low fields, weakens in high fields, and, critically, is strongly suppressed for in-plane fields (data not shown).

The existence of what is effectively metallic 2D transport [63–65] in sample B is significant, as it enables a simple upper bound to be placed on the thickness of the surface conductive layer. Specifically, 2D electronic behavior requires $t_s < \lambda$, where t_s is the thickness of the conducting region, and λ is the mean-free path [66]. Within a simple Drude model, the relation $\lambda = v_F\tau$ (where v_F is the Fermi velocity and τ is the momentum relaxation time), can be combined with $\mu = e\tau/m^*$ (where m^* is the carrier effective mass), to write $\lambda = \frac{v_F m^* \mu}{e}$. For a 2D free electron gas with areal carrier density n_{2D} and Fermi wave vector $k_F = (2\pi n_{2D})^{1/2}$, we can then use $v_F = \hbar k_F/m^*$ to write $v_F = \frac{\hbar}{m^*}\sqrt{2\pi n_{2D}}$, yielding

$$\lambda = \frac{\hbar\mu}{e}\sqrt{2\pi n_{2D}}. \quad (2)$$

Inserting the values of 2D carrier density and surface mobility extracted below (Sec. III D) from Hall effect measurements on this sample (1.8×10^{14} cm^{-2} and 6 cm^2 V^{-1} s^{-1}) yields $\lambda = 1.8$ nm, placing a rough upper bound on t_s of 1.8 nm, i.e., ~3 unit cells. It is interesting to compare this to prior estimates from other approaches. These include 0.7 nm based on where deviations from bulk density-of-states occur in first-principles calculations [41], 1.3 nm based on space-charge analysis of electrochemical impedance spectroscopy data [14], and 4.4 nm based on space-charge analysis of experimental energy levels and band alignments [27]. Our estimate is thus consistent with these prior ones, indicating, importantly, that the conductive surface layer on pyrite single crystals is nanoscopic.

Analysis of $R(T, B_\perp)$ in sample G, on the insulating side of the IMT, yields similarly important insights, in addition to an independent confirmation of our t_s estimate. In this insulating sample, $R(T)$ from the lowest measurable temperatures to ~100 K follows

$$R = R_0 \exp\left[\left(\frac{T_0}{T}\right)^{1/2}\right], \quad (3)$$

as illustrated in Fig. 5(d). This is the behavior characteristic of Efros-Shklovskii (ES) variable range hopping (VRH), where R_0 is the $T \to \infty$ extrapolation of R, T_0 is a characteristic temperature scale dictated by the (doping-dependent) dielectric constant and localization length, and the formula applies in all dimensions [59]. Although the straight line fit in Fig. 5(d) is very satisfactory, ES VRH was further confirmed, in an unbiased manner, via the Zabrodskii analysis shown in the inset to Fig. 5(d) [67]. This involves plotting ln W vs ln T, where $W = -d(\ln R)/d(\ln T)$, thus linearizing the generalized from of Eq. (3), $R = R_0 \exp[(\frac{T_0}{T})^m]$ [67]. The exponent m is then extracted directly as the negative slope of the resulting straight line. As shown in the figure, a straight line with negative slope is indeed obtained in this T range, resulting in $m = 0.57$, close to the value of 1/2 expected for ES VRH. The extracted T_0 of 1300 K is moderately large, indicating VRH quite deep in the insulating regime, as expected from the qualitative form of $R(T)$ for this sample [see Fig. 3(b), sample G]. Significantly, that VRH is active in this sample at low T then naturally explains the positive MR found in perpendicular fields at low T [see Fig. 5(a), sample G]. This MR is shown at the representative T of 30 K in Fig. 5(e), where $\ln(R/R_{B=0})$ is plotted vs $B_\perp$. As illustrated by the fit (solid line), the data closely follow

$$\ln\left(\frac{R}{R_{B=0}}\right) = \frac{s}{\hbar^2} L_c^4 B_\perp^2 \left(\frac{T_0}{T}\right)^{3/2}, \tag{4}$$

where $R_{B=0}$ is the resistance in zero field, s is a numerical constant (0.0015), and L_c is the carrier localization length [59]. Using the $T_0 = 1300$ K determined from $R(T)$, this fit yields $L_c = 3.4$ nm, revealing strongly localized states, consistent with transport deep on the insulating side of the IMT. Both $R(T)$ and $R(B_\perp)$ at low T for sample G are thus consistent with 2D surface-dominated transport via ES VRH, indicating conduction through Coulomb-gapped defect states.

The L_c value extracted from $R(B_\perp)$ for this sample, which has a semiconducting surface layer, provides an additional independent estimate of an upper bound on t_s. Specifically, L_c, in combination with T_0, provides the average hopping length $L_{hop}(T)$ via [59]

$$L_{hop} = \frac{1}{4} L_c \left(\frac{T_0}{T}\right)^{1/2}. \tag{5}$$

Given the 2D nature of the IMT in this system [Fig. 4(c)], and the 2D nature of the low T conduction on the metallic side of the IMT (in sample B), we assume similar two dimensionality of the hopping conduction in sample G. For this to be so, $L_{hop} > t_s$ must be obeyed, providing an independent upper bound on t_s. Applying Eq. (4) at 100 K, i.e., the highest T at which ES VRH could be established, then yields $L_{hop} = 3$ nm, and thus a 3 nm upper bound for the thickness of the surface transport layer. We use the highest reasonable T in this estimate as there is no obvious reason to expect a T-dependent t_s, and this generates the most stringent upper bound (lowest L_{hop}). Given the assumptions made, the two t_s estimates of 1.8 and 3 nm are in reasonable agreement, both falling within the range of prior estimates (0.7 to 4.4 nm) [14,27,41].

D. Electronic transport: Hall effect measurements

Hall effect measurements are presented next, to determine bulk and surface carrier densities and mobilities, and to probe any potential inversion from n to p type on cooling to the surface-dominated regime. To this end, Fig. 6 shows the Hall resistance (R_{xy}) vs $B_\perp$ for samples B, G, Y, and R, at three representative T in each case. Note that zero field backgrounds have been subtracted from these data, and that MR contamination has been carefully corrected for following standard practices. Starting with sample B, which has $T_{cr} \approx 145$ K [Fig. 3(b)] and a surface exhibiting transport near the IMT [see Figs. 4(c), 5(b) and 5(c)], the 270 K Hall signal is seen to be linear, with a negative Hall coefficient $R_H = tR_{xy}/B_\perp$ (where t is the sample thickness). This indicates that the bulk conduction in this sample is clearly n type, with no obvious indication of multiple carrier types; simple interpretation ($R_H = -1/|n|e$) yields an electron density $n = 4.4 \times 10^{16}$ cm^{-3}. Qualitatively similar behavior is shown in Fig. 6 for samples G and Y, giving $n = 1.1 \times 10^{16}$ and 1.7×10^{17}cm^{-3}, respectively. No corresponding extraction of the 270 K Hall density is attempted at this stage for sample R, which, as discussed, does not exhibit purely bulk transport even at 270 K. n-type behavior is nevertheless suggested for this sample from Fig. 6(j), and in fact all crystals measured in this study were found to be n type at high T, consistent with recent work on unintentionally doped pyrite crystals. We [25], and others [3,14,27], have speculated that this bulk n doping arises from V_S, although additional verification is needed. Quantitatively, the room temperature bulk electron mobilities (115−150 cm^2 V^{-1} s^{-1}) are comparable to recent reports, while the corresponding Hall electron densities ($\sim 10^{16}-10^{17}$ cm^{-3}) are somewhat higher [14,27].

As shown in Figs. 6(a)–6(c), sample B provides an important advance in the understanding of surface conduction in pyrite by providing exemplary evidence for an $n \to p$ crossover as the transition from bulk- to surface-dominated transport takes place. At a representative T of 133 K, for example, close to T_{cr}, the Hall effect becomes strikingly nonlinear, the electronlike low field behavior giving way to holelike behavior at higher fields. At 5 K, deep in the surface-dominated regime, the Hall effect then clearly inverts, presenting linear behavior and a positive R_H. We emphasize that this inversion occurs here in a sample with a surface layer that is essentially metallic, or at most weakly localized [see Figs. 3(b), 4(a), and 5(b)], with no possibility of hopping conduction at these temperatures. This is an important advance over prior work [27] as it demonstrates a p-type surface inversion layer with no possibility of sign inversion artifacts [20,23,25,29–32] from hopping. Additionally, we show below that the observation of nonlinear Hall effect in the crossover regime is not only just as expected, but can also be used to significantly constrain a two-channel model of the transport in these crystals.

The complications that arise due to hopping conduction are well illustrated by sample G [Figs. 6(d)–6(f)], which, as already noted, exhibits similar behavior to recently studied mechanically polished crystals [27]. While we find nonlinearity in $R_{xy}(B_\perp)$ around T_{cr}, which was not detected in prior work, the low T (30 K) Hall behavior is similar

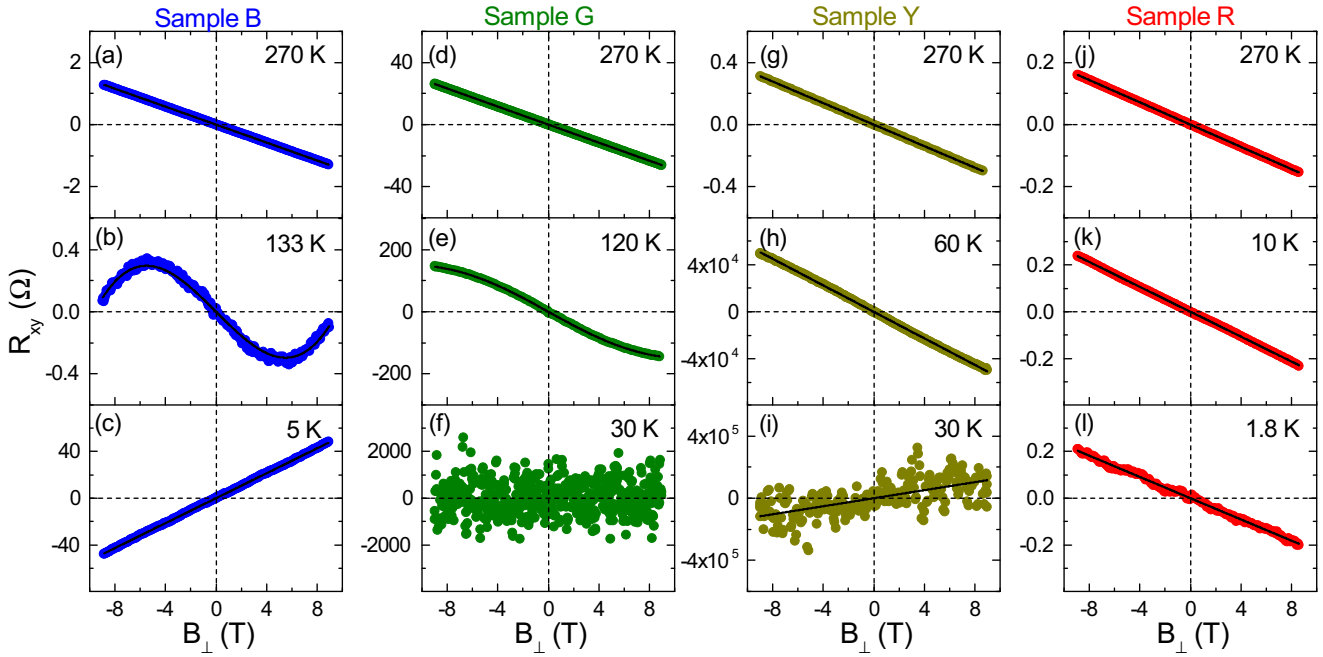

FIG. 6. Magnetic field dependence of the Hall effect. The transverse resistance (R_{xy}) is shown vs the out-of-plane magnetic field $B_\perp$ at representative temperatures for samples B (a)–(c), G (d)–(f), Y (g)–(i), and R (j)–(l). Temperatures are shown in the upper right corner, descending from top to bottom. The solid black lines through the data are fits to the nonlinear two-channel conduction model described in the text.

to that of Limpinsel *et al.* [27], presenting a diminished Hall signal that is essentially at or below the measurement noise floor. [The noise in Fig. 6(f) is $O(10\ \mu\text{V})$, on a dc measurement at a four terminal resistance value of 2 MΩ]. As established by Figs. 5(d) and 5(e), the low T (i.e., surface-dominated) conduction in this sample, which is $\sim 10^4$ times more resistive than sample B at 30 K, occurs unambiguously via ES VRH, meaning that small R_H is expected. As noted in the Introduction, the Hall effect is suppressed in hopping conductors, and no longer even reliably reflects the true sign of the majority charge carriers [20,23,25,29–32]. As discussed below, quantitative analysis of additional T-dependent Hall data does nevertheless support an inverted surface in sample G, consistent with the nonlinearity in Fig. 6(e). A not dissimilar picture emerges from Figs. 6(g)–6(i), for sample Y, where the low T_cr and high resistivity combine to make measurement and interpretation of the Hall effect in the low T regime again nontrivial. The signal-to-noise ratio in the Hall data at low T is modest, with hopping conduction also a possibility, due to the small available surface-dominated temperature window in this sample [see Fig. 3(b)], making accurate assessment of the form of $R(T)$ below T_cr difficult. Nevertheless, holelike behavior is indicated at 30 K [Fig. 7(i)] in addition to weak nonlinearity in $R_{xy}(B_\perp)$ at 60 K, both suggesting p-type surface inversion. This is further supported below by quantitative analysis of additional T-dependent Hall data. Finally, sample R again provides a surprising result. Despite exhibiting surface-influenced conduction at essentially all T probed in this work [Figs. 3(b) and 4(a)], this sample exhibits a Hall effect [Figs. 6(j)–6(l)] that is *unambiguously n type at all T*. Surface conduction of n-type character has not been previously reported in pyrite to the best of our knowledge, and was revealed here only by the measurement of the diverse surface transport behavior of as-prepared surfaces.

$R_{xy}(B_\perp)$ measurements of the type shown in Fig. 6 were acquired at additional T between 300 and 1.5 K, and are now analyzed quantitatively. We start with samples B, G, and Y, specifically at high T, well above T_cr, where bulk conduction clearly dominates. R_{xy} is always linear in $B_\perp$ under these conditions [as in Figs. 6(a), 6(d), and 6(g)], and we assume $n \gg p$ (i.e., dominance of bulk electrons) to extract the bulk electron density and mobility from $n_\text{b}(T) = [eR_\text{H}(T)]^{-1}$ and $\mu_\text{b}(T) = R_\text{H}(T)/\rho$. The results are shown in Fig. 7, the top two panels of which plot the T dependence of the carrier densities and mobilities for samples B, G, Y, and R. Explicitly, the top panel of this figure plots the bulk and surface electron or hole densities, the next panel down plots the bulk and surface electron or hole mobilities, the panel below that reproduces $\rho(T)$ for comparison, and the bottom panel displays the magnitude of the low field R_H, all of which are discussed in this section. Solid points in this figure denote n-type behavior, open points p-type behavior, circles bulk parameters, and triangles surface parameters, as shown in the legend. Focusing first on samples B, G, and Y, and on the (high T) bulk Hall electron densities and mobilities, Figs. 7(a), 7(e), and 7(i) and Figs. 7(b), 7(f), and 7(j) show $n_\text{b}(T)$ and $\mu_\text{b}(T)$. As might be expected, clear carrier freeze-out is apparent in $n_\text{b}(T)$ [Figs. 7(a), 7(e), and 7(i)], the solid lines being fits to a simple activated form $n_\text{b} = N_\text{b} \exp(-E_\text{b}/k_\text{B}T)$, where N_b is the $T \to \infty$ extrapolation of n_b, and E_b is the activation energy. This is found to describe the data well at all T at which bulk conduction is relevant, for all three samples, with $\mu_\text{b}(T)$ correspondingly rising on cooling from 300 K [Figs. 7(b), 7(f), and 7(j)]. Further discussions and analyses of $n_\text{b}(T)$ and $\mu_\text{b}(T)$

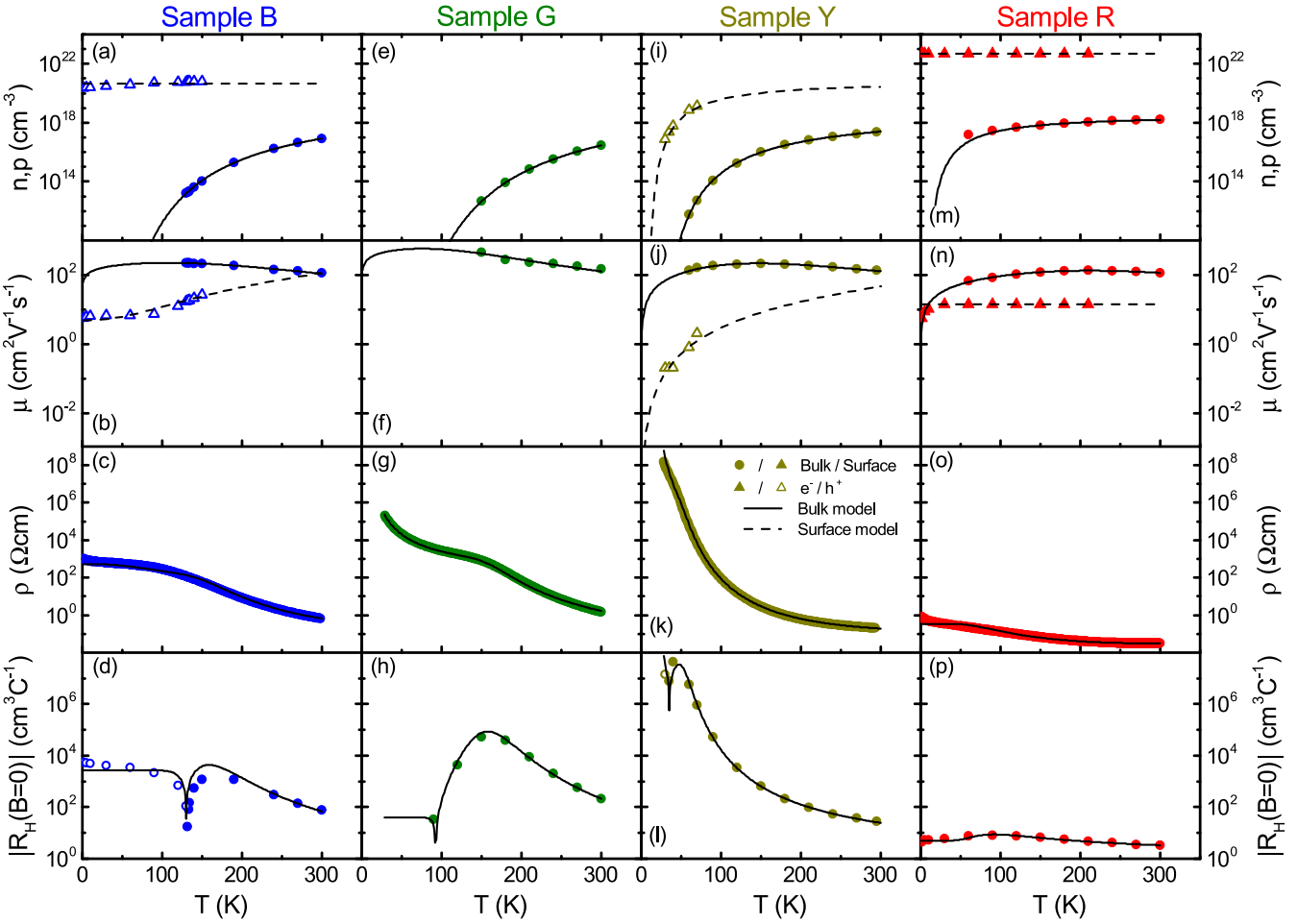

FIG. 7. Temperature dependence of the carrier densities, mobilities, resistivities, and Hall coefficients, along with two-channel conduction model results. (a), (e), (i), and (m) Temperature dependence of the electron or hole density (n or p) from fitting of the Hall effect data for samples B, G, Y, and R, respectively. In all panels, circles (triangles) represent bulk (surface) values, and closed (open) symbols represent electrons (holes). In all panels, the solid and dotted black lines represent the two-channel conduction model fits, resulting in the parameters summarized in Table I. (b), (f), (j), and (n) Temperature dependence of the Hall mobilities (μ) for samples B, G, Y, and R, respectively. (c), (g), (k), and (o) Temperature dependence of the resistivity (ρ) for samples B, G, Y, and R, respectively. (d), (h), (l), and (p) Temperature dependence of the magnitude of the low-field Hall coefficient [$R_H(B = 0)$], for samples B, G, Y, and R, respectively.

are provided below, after first discussing the full T range of the Hall data.

Analysis of Hall effect data in samples B, G, and Y at the lowest T, well below T_{cr}, is also relatively straightforward. In this regime surface conduction dominates, $R_{xy}(B_\perp)$ is again linear [Figs. 6(c), 6(f), and 6(i)], and we can extract the surface hole density and mobility from $p_s(T) = [eR_H(T)]^{-1}$ (where $R_H = t_s R_{xy} B_\perp$) and $\mu_s(T) = R_H(T)/\rho$. This directly yields, however, only the mobility and the *two-dimensional* (i.e., areal) hole density, that is, the product $p_s t_s$. Extraction of the *three-dimensional* hole density in the surface layer requires that the thickness of the surface layer is defined. For simplicity we fix this at $t_s = 3$ nm, based on the larger of the two upper bound estimates above, meaning that the deduced p_s values should be viewed as lower bounds. Figure 7(a) shows the resulting $p_s(T)$ for sample B, which reveals essentially T-independent values in the 10^{20} holes/cm^3 range. These high, T-independent hole densities are of course consistent with the weak low temperature $R(T)$ for this sample, as reproduced in Fig. 7(c), reflecting the essentially metallic surface behavior. The low T values of μ_s lie at $\sim$10 cm^2 V^{-1} s^{-1}, and are again only weakly T dependent. No corresponding analysis is possible for sample G because R_H is suppressed at low T due to VRH; Figs. 7(e) and 7(f) thus show no $p_s(T)$ and $\mu_s(T)$ data. In sample Y, however, the small positive R_H of the type shown in Fig. 6(i) can be analyzed, resulting in $p_s(T)$ that freezes-out rapidly [Fig. 7(i)], accompanied by a μ_s that falls on cooling. The $p_s(T)$ behavior in this crystal is thus very different to that of sample B, consistent with the more insulating form of $R(T)$, as reproduced in Fig. 7(k); low T surface hole mobilities in this sample [Fig. 7(j)] are also correspondingly lower. Finally, sample R can also be analyzed in this manner at low T. Here the surface carriers are electrons, as shown in Fig. 6(l), the T dependence of n_s [Fig. 7(m)] revealing an essentially constant value of $\sim 10^{23}$ cm^{-3}, with a correspondingly flat $\mu_s(T)$ at $\sim$10 cm^{2}V^{-1}s^{-1}. These surface electron densities border on unphysically high values, of course, potentially providing a clue as to the origin of the unusual properties of crystals exemplified by sample R, as returned to below.

TABLE I. Summary of the parameters extracted from the two-channel (surface and bulk) conduction model for samples B, G, Y, and R. Bulk and surface parameters are labeled using "b" and "s" subscripts, respectively. E denotes activation energies, N is the infinite temperature extrapolations of the electron or hole densities, α are the high temperature exponents in $\mu \propto T^{-\alpha}$, β are the low temperature exponents in $\mu \propto T^{\beta}$, and $\mu_{s,T=0}$ are the zero temperature surface mobilities. For N_s, negative and positive values denote electrons and holes, respectively.

Parameters	Sample B	Sample G	Sample Y	Sample R
E_b (meV)	170	226	84	22
N_b(cm^{-3})	6.0×10^{19}	1.8×10^{20}	6.6×10^{18}	3.7×10^{18}
α_b	2.5	2	2.0	2.5
β_b	0.3	2.1	1	0.8
E_s (meV)	0	–	26	0
N_s(cm^{-3})	$+1.1 \times 10^{21}$	$+1.1 \times 10^{22}$[a]	$+1.3 \times 10^{21}$	-8.3×10^{22}
β_s	2.5	–	2.5	–
$\mu_{s,0}$(cm^2 V^{-1} s^{-1})	5	–	0	14.3

[a]As discussed in the text, the N_s value for sample G cannot be directly interpreted as a carrier density due to hopping conduction. The value listed is simply the $(eR_H)^{-1}$ value that produces a good fit to the temperature dependence of $|R_H|(B = 0)$, as shown in Fig. 7(h).

Having analyzed and discussed the behavior in the high and low T limits, in which the bulk and the surface dominate, respectively, we now turn to analysis at intermediate T, around T_{cr}, where both contribute. As in Limpinsel *et al.* [27] we achieve this by employing a two-channel (i.e., surface and bulk) conduction model, generalized in our case to include field dependence in R_H [57]. This model treats the bulk and surface as parallel resistors, with their own carrier densities and mobilities. Note here that by "surface" we refer primarily to the top (as-grown) surface, not explicitly including contributions from the bottom (polished) side of the crystal. This is a particularly safe assumption in the case of samples of type B and R, as their surfaces exhibit substantially lower resistance than any polished surface measured, thus shunting the current. In cases such as samples G and Y, the backside could indeed contribute to the low temperature conduction, but the relatively similar resistance behavior exhibited by all polished surfaces render these effects modest. The total conductivity (σ) can then be written:

$$\sigma = \frac{|e\mu_b n_b t_b| + |e\mu_s p_s t_s|}{t}, \tag{6}$$

where t_b is the thickness of the bulk region and t is the total thickness, such that $t_b + t_s = t \approx t_b$. The Hall resistance is then given by

$$R_{xy} = \frac{R_H B_\perp}{t}, \tag{7}$$

where the field-dependent Hall coefficient is

$$R_H = \frac{t}{e} \frac{p_s t_s \mu_s^2 - n_b t_b \mu_b^2 + \mu_s^2 \mu_b^2 (p_s t_s - n_b t_b) B_\perp^2}{(\mu_s p_s t_s + \mu_b n_b t_b)^2 + \mu_s^2 \mu_b^2 (p_s t_s - n_b t_b)^2 B_\perp^2}. \tag{8}$$

Our derivation of (8) is outlined in the Supplemental Material [57]. Note again here that the parameters t_s and p_s are coupled in these equations (they appear as a product), meaning that extraction of a 3D hole density in the surface layer requires knowledge of t_s. As above, we use $t_s = 3$ nm, for the reasons already elaborated. Equations (6)–(8) then give the two experimentally measured quantities, $\sigma(T)$ and $R_{xy}(B_\perp, T)$, in terms of four fitting parameters n_s, p_s, μ_s, and μ_b. In our case the measurement of the field dependence of the nonlinear Hall effect places significant additional constraints on the fitting parameters in comparison to earlier work [27]. We thus proceed by fitting $R_{xy}(B_\perp)$ at each individual T for each sample. As shown in Fig. 6 the resulting fits (solid lines) are very good, meaning that Eqs. (7) and (8) indeed accurately capture the evolution of the nonlinear Hall effect through the bulk-to-surface crossover. Yet further constraint on the fitting parameters can be added for samples B, G, and Y by constraining $n_b(T)$ to take the activated form observed at $T \gg T_{cr}$, i.e., $n_b = N_b \exp(-E_b/k_B T)$, at all T. For sample R, on the other hand, p_s (which is negative for n-type surfaces) was found to be negligibly T dependent for $T \ll T_{cr}$, and was thus held constant at all T.

The resulting full T dependencies of μ_s, p_s, μ_b, and n_b for the four samples are shown in the top panels of Fig. 7. Note here that bulk (surface) data points are shown only in the T range over which a significant contribution from the bulk (surface) occurs. There are also no surface transport parameters reported for sample G, due to the aforementioned VRH-suppressed low-T Hall coefficient [Fig. 6(f)]. With these points in mind, quantitative analysis of the T dependence of the bulk and surface carrier densities is now presented. Starting with the bulk first, as already noted, $n_b(T)$ can be fit to $n_b = N_b \exp(-E_b/k_B T)$, the solid lines in Figs. 7(a), 7(e), 7(i), and 7(m) resulting in the E_b and N_b values in Table I. This table in fact provides a full summary of the parameters extracted from analysis of Figs. 6 and 7. The E_b values for samples B, G, and Y lie in the 80–230 meV range, with corresponding N_b's between 7×10^{18} and 2×10^{20} cm^{-3}. This is broadly consistent with recent prior work on pyrite crystals [14,27], the 230 meV seen in sample G, for instance, being close to that seen by Limpinsel *et al.*, potentially reflecting a V_S deep donor level. The E_b value for sample R, however, is only 22 meV, reflecting the weak T dependence seen in $n_b(T)$ for this sample, consistent with its higher 300 K electron density of $\sim 10^{18}$ cm^{-3}. The latter is substantially larger than the other classes of samples studied here, and we make two important points about this. First, while purely bulk transport does not occur in this sample even at 300 K, at this T the two-channel analysis suggests >90% of the current flows through the bulk.

We thus have reasonable confidence in the extracted bulk transport parameters. Second, we note again that the unusual behavior of sample R is *not* correlated with unusually high or low Ni impurity concentration. The lack of any correlation between Ni impurity concentration and transport behavior in this work may indicate that Ni is not an n-dopant in FeS_2, consistent with recent work [68]. Additional research to verify this would clearly be interesting and worthwhile.

Turning now to *surface* carrier densities, and beginning with sample B, as already noted the low T behavior of $p_s(T)$ in this case is essentially flat, consistent with practically 2D metallic behavior. No corresponding surface carrier densities are available for sample G, while sample Y presents $p_s(T)$ that exhibits freeze-out, consistent with the semiconducting nature of this sample's surface. Sample R, on the other hand, has an n-type surface, again with negligible T dependence of the carrier density. In all cases the T dependence of the surface carrier density can be well described by simple activation, the dashed lines in Figs. 7(a), 7(e), 7(i), and 7(m) being fits to $p_s = N_s \exp(-E_s/k_B T)$, where N_s is the $T \to \infty$ value of p_s, and E_s is the surface activation energy. As shown in Table I, the E_s value for sample B is zero (the surface is effectively metallic), the E_s for sample Y is 26 meV (a relatively small activation energy, much lower than the bulk), while the E_s for sample R is again zero (again, effectively metallic). Table I additionally shows the N_s values, which for samples B and Y are $\sim 1 \times 10^{21}$ cm^{-3}. The equivalent N_s for sample R, which is shown in Table I as negative to highlight the n-type surface conduction, is much larger, consistent with the earlier comment about surface electron densities in this class of samples approaching unphysical levels; this is returned to below.

Moving on to analysis of the T dependence of the mobilities, and again beginning with the bulk, Figs. 7(b), 7(f), 7(j), and 7(n) show that the form of $\mu_b(T)$ is quite consistent across all four samples. A rise on cooling from 300 K, before a decrease at low T, is commonplace in relatively heavily doped semiconductors, arising due to a competition between phonon and ionized impurity scattering [69]. This can be captured in our case with mobilities in the high and low T limits that follow power law behavior:

$$\mu(T \to 300\ \mathrm{K}) \propto T^{-\alpha_b} \tag{9}$$

and

$$\mu(T \to 0) \propto T^{\beta_b}, \tag{10}$$

where α_b and β_b are (bulk) exponents. The $T^{-\alpha_b}$ form is a standard approach to describing phonon scattering at high T, while the low temperature T^{β_b} dependence is a simple means to parametrize the ionized impurity scattering sometimes modeled in the Conwell-Weisskopf or Brooks-Herring approaches [70,71]. Based on Matthiesen's rule, the mobility at any T can then be modeled with $\mu_b(T) \propto \frac{\mu(T \to 300\ \mathrm{K})\mu(T \to 0)}{\mu(T \to 300\ \mathrm{K}) + \mu(T \to 0)}$, a process that works well for all crystals in this study [see the solid fit lines in Figs. 7(b), 7(f), 7(j), and 7(n)]. As shown in Table I, the resulting α_b values vary little between samples, falling between 2.0 and 2.5 in all cases. This is consistent with prior reports [27,72], where typical values were 2.5, potentially associated with optical phonon scattering [69]. The β_b values vary more widely, falling between 0.3 and 2.1, although we note that these derive from the limited T range over which the T^{β_b} behavior can be probed before surface conduction interferes, and eventually dominates; these values should therefore not be over-interpreted. The surface mobilities shown in Figs. 7(b), 7(j), and 7(n) can be described in a similar fashion to $\mu_b(T)$, simply by adding a constant $\mu_{s,T=0}$ to capture the finite $T \to 0$ extrapolation of the conductance for the crystals with effectively metallic surfaces, i.e., samples B and R. The low T behavior thus becomes $\mu_s(T) = \mu_{s,T=0} + cT^{\beta_s}$, where c is a constant. The resulting fits [dashed lines in Figs. 7(b), 7(j), and 7(n)] yield the parameters shown in Table I, where finite $\mu_{s,T=0}$ values are found only for samples B and R, as expected. In the two samples in which non-negligible T dependence of μ_s is found (samples B and Y) the β_s values extracted from the data were identical, at 2.5.

Importantly, with the T dependence of μ_s, p_s, μ_b, and n_b fully parametrized, Eq. (6) can then be used in conjunction with the parameters from the fitting of the Hall data to compute $\sigma(T)$, for comparison with the measured $\rho(T)$. As shown in Figs. 7(c), 7(g), 7(k), and 7(o) this self-consistency check produces satisfying results, the solid lines [from Eq. (6)] coinciding well with the measured $\rho(T)$. Using Eq. (8), a similar process can be followed to calculate the T dependence of $|R_H|(T)$ in the $B_\perp \to 0$ limit, as shown in Figs. 7(d), 7(h), 7(l), and 7(p). The solid lines here result from the parameters shown in Table I, using a fitted T-independent surface value of $R_H = 50\,\mathrm{cm^3 C^{-1}}$ for sample G, where no data are directly available; a similar approach was used in Fig. 7(g). In all cases, Figs. 7(d), 7(h), 7(l), and 7(p) show satisfactory agreement, the model reproducing the diverse behavior of the experimental $|R_H(B_\perp \to 0)|(T)$ in the four crystals, including the sharp minima across the bulk to surface crossovers. The presented two-channel conduction model thus reproduces all available transport data on the four representative crystals discussed in this paper.

IV. DISCUSSION AND OPEN QUESTIONS

The existence of surface conduction in the CVT-grown pyrite single crystals studied here appears undeniable based on the above results and analysis. Surface conduction is apparent from the unusual $R(T)$ (i.e., the existence of T_{cr}), the nonmonotonic $A_{vdP}(T)$, the thickness scaling of $R(T)$, the extreme sensitivity of low T transport to surface preparation, and the deduced 2D nature of the IMT. Surface transport effects are thus not confined to FeS_2 crystals grown by a specific method [27], but are more general. Transport substantially different from the bulk apparently occurs in a region that is typically restricted to within 2–3 nm of the surface, albeit with substantial variations in the nature of that surface conduction. At as-grown surfaces with atomic-scale roughness the surface behavior varies from effectively metallic with degenerate doping of $\sim 10^{21}$ cm^{-3} and a $T \to 0$ mobility of 5 cm^2 V^{-1}s^{-1} (as in sample B), to semiconducting with an activation energy $\sim$20 meV and mobility $<0.1\,\mathrm{cm^2\,V^{-1}\,s^{-1}}$ at 30 K (as in sample Y). The progression from samples B $\to$ G $\to$ Y thus involves surface conduction that crosses from weakly localized

2D transport to ES VRH deep on the insulating side of the IMT. The surface majority carrier type in such crystals is also inverted with respect to the bulk, being definitively *p* type. This conclusion is reached from the study of samples in which the transport clearly does not involve hopping conduction, and is thus robust. The nonlinear Hall effect observed at the T-dependent bulk to surface crossover in such samples is also as expected at such a crossover and can be used to tightly constrain a two-channel conduction model capable of capturing all quantitative features of the measured transport. While the extracted surface transport parameters vary widely (as expected from the above), the bulk parameters for samples in classes B, G, and Y reveal doping levels, mobilities, and activation energies that are relatively consistent, and in reasonable agreement with prior work.

A number of important questions emerge from these findings. First, and as already noted, it seems imperative that additional research be undertaken to more definitively determine whether V_S are indeed responsible for *n*-type bulk behavior in unintentionally doped FeS_2 single crystals. This is a vital step to understand and control doping in pyrite, which is essential to unlock the full PV potential of this material. Second, it indeed appears likely at this stage that surface effects could have played a major role in the failure of earlier pyrite-based solar cells [27], certainly the ones based on single crystals. The *origin* of the surface conduction is thus of course a central issue. We first note that the *p*-type character of the majority of the surfaces studied here is generally consistent with prior work based on x-ray/ultraviolet photoelectron spectroscopy [3,8,9,20,27,73–75], transport [27], and other methods [14]. Photoelectron spectroscopy leads to the conclusion that the most likely origin of the heavy *p*-type surface doping, and associated Fermi level pinning near the valence band, is *intrinsic* surface states [8,9,73–75]. The important model of Bronold *et al.* considered stoichiometric (001) FeS_2 surfaces and found the fivefold surface coordination of Fe causes the Fe $3d_{z^2}$ (e_g) orbital to fall into the band gap, creating an intrinsic surface state [8,9]. Nesbitt *et al.* later reevaluated the Bronold model, finding the inclusion of monosulfide species (i.e., nonstoichiometric (100) $FeS_{2-\delta}$) to better describe the S $2p$ spectrum [73,74]. Andersson *et al.* subsequently used Ne^+ sputtering to control the monosulfide defect density and thus the S $2p$ spectra [73,75]. This latter fact is noteworthy for our work, as the surface S stoichiometry could vary in our crystals as a consequence of varied cooling rates and sulfur overpressures during CVT growth, even within a single growth tube, due to unavoidable temperature gradients, etc. Before moving on, we note again that surface states could be generic to pyrite structure transition metal disulfides, due to indications in CoS_2 and NiS_2.

Alternatively, some ubiquitous surface dopant could be responsible for the *p*-type surface inversion layer. While more work is needed, one speculative possibility is the incorporation of Br^- during growth, or some atmospheric impurity such as oxygen, potentially at V_S sites. As already noted, no measurable Br signal is observed in our PIXE measurements, although the $\sim 10\,\mu$m sampling depth renders PIXE a bulk probe relative to the ~ 3 nm surface layer. A method such as depth-profiled secondary ion mass spectrometry could potentially better elucidate this issue. Whether O specifically could behave as an acceptor in pyrite is debated from the theoretical perspective [43,76], although we note that theoretical studies of the recently discovered high pressure pyrite FeO_2 phase [77] suggest an Fe valence [78] that might support *p* doping in $FeS_{2-x}O_x$. Additional theoretical work would be worthwhile here, as would experimental efforts at O doping. Careful depthwise investigations of impurity incorporation, coupled with transport measurements, would also be beneficial. Returning to *intrinsic* surface possibilities, while it seems unlikely based on the weak spin-orbit interaction expected, and the relatively large band gap (although this could be lowered at the surface), the possibility of a topological insulator state should perhaps be ruled out in FeS_2. First-principles electronic structure calculations should be able to confirm that the band structure is topologically trivial, while experimental studies with angle-resolved photoemission spectroscopy could rule out the characteristic behavior of a topological insulator [48–51]. This would avoid the irony of working to avoid surface conduction phenomena in a material in which they are topologically protected.

Just as important as the origin of the *p*-type surface inversion in pyrite is the question of the *impact* of this behavior. From the perspective of PV devices, for example, it seems essential to understand how the band profile that results from surface inversion influences V_{oc}. This is a point upon which there is some disagreement in the literature, some work suggesting that the *p*-type surface leads to the formation of deleterious leaky tunnel barriers [6,8,27], some concluding that is the deep donors (potentially from V_S) that are the key culprit in poor solar cell performance [14]. The deduced band profiles are nevertheless similar in these two cases, as are the essential ingredients (dense surface acceptors and bulk donors). While additional heterojunction studies incorporating well-controlled FeS_2 single crystal surfaces would clearly help understand this point further, one additional avenue that could yield improved understanding is the electrical characterization of the internal *p*-*n* junction implicated by the results provided here. Future work combining in-plane and through-plane (i.e., vertical) transport could elucidate this important issue. It should be added that the interplay of the above issues with the band gap narrowing that has been evidenced at FeS_2 surfaces [40] is another open question.

Finally, there is of course the issue of potential means to *control* the surface conduction established here. In this respect our observation of substantial diversity in surface transport behavior in nominally identical as-grown crystals is important, as the factors that generate the diversity in surface doping and mobility remain to be understood. Future work establishing structure-property relationships for surface transport would clearly be desirable, and could include the full battery of surface structural and chemical characterization techniques, including scanning probe microscopy and photoemission-based methods. Scanning tunneling microscopy and spectroscopy, conductive probe AFM, and Kelvin probe microscopy [14] could be particularly fruitful given the nature of this problem. Along these lines, the crystals in this work exemplified by sample R are particularly intriguing. These exhibit degenerately doped metallic surfaces that are *not* inverted with respect to the bulk, their resistance being so low that purely bulk transport does not occur in in-plane measurements even

at 300 K. While further work is needed to understand this behavior, potentially via the various avenues discussed above, one immediate possibility is that the t_s value in such crystals is significantly larger than in more typical ones. This is suggested by the nearly unphysical surface electron densities deduced by assuming $t_s = 3$ nm, which would reduce to more reasonable values if t_s were anomalously high. It is interesting to note that the low T resistance of samples in class R are in fact the lowest shown in Fig. 4(c), approaching the vertical gray dashed line that marks the position of the *three-dimensional* IMT. Again, additional work is required to explore this possibility, including understanding the possible connection to the unusually high *bulk n* doping in such samples.

V. SUMMARY

In summary, a detailed electronic transport study of a large set of thoroughly structurally and chemically characterized pyrite FeS_2 single crystals has been undertaken in this work. Surface conduction phenomena are ubiquitous in such crystals, manifesting themselves in the temperature, thickness, and magnetic field dependence of the resistivity and Hall effect, and enabling estimates of the thickness of the nanoscopic surface conductive layer. This layer is found to have quite diverse transport character, even in nominally identical as-grown crystals, a feature that is suppressed by mechanical polishing of the surface. The surface of such crystals is also typically p type, being inverted from the bulk, a conclusion that is reached even in samples that do not exhibit hopping conduction. The nonlinear Hall effect induced by this inversion has been shown to be consistent with a simple two-channel conduction model, which captures all aspects of the transport behavior found here. These findings, and the open questions they highlight, have been discussed in detail. It is suggested that while surface electronic effects are gradually yielding to understanding in pyrite FeS_2, substantial additional work will be required to understand and control them, a critical step in unlocking the photovoltaic potential of this fascinating material.

ACKNOWLEDGMENTS

This work was supported by the customers of Xcel Energy through a grant from the Renewable Development Fund, by the National Science Foundation (NSF) through the University of Minnesota MRSEC under DMR-1420013, and by the NSF under DMR-1309642. Parts of this work were carried out in the Characterization Facility, University of Minnesota, which receives partial support from NSF through the MRSEC program. We thank K. Reich and B. Shklovskii for informative discussions.

[1] C. A. Wolden, J. Kurtin, J. B. Baxter, I. Repins, S. E. Shaheen, J. T. Torvik, A. A. Rockett, V. M. Fthenakis, and E. S. Aydil, Photovoltaic manufacturing: Present status, future prospects, and research needs, J. Vac. Sci. Technol. A **29**, 030801 (2011).

[2] C. Wadia, A. P. Alivisatos, and D. M. Kammen, Materials availability expands the opportunity for large-scale photovoltaics deployment, Environ. Sci. Technol. **43**, 2072 (2009).

[3] A. Ennaoui, S. Fiechter, C. Pettenkofer, N. Alonso-Vante, K. Büker, M. Bronold, C. Höpfner, and H. Tributsch, Iron disulfide for solar energy conversion, Sol. Energy Mater. Sol. Cells **29**, 289 (1993).

[4] A. Ennaoui and H. Tributsch, Iron sulphide solar cells, Sol. Cells **13**, 197 (1984).

[5] A. Ennaoui, S. Fiechter, W. Jaegermann, and H. Tributsch, Photoelectrochemistry of highly quantum efficient single-crystalline n-FeS_2 (pyrite), J. Electrochem. Soc. **133**, 97 (1986).

[6] K. Büker, N. Alonso-Vante, and H. Tributsch, Photovoltaic output limitation of n-FeS_2 (pyrite) Schottky barriers: A temperature-dependent characterization, J. Appl. Phys. **72**, 5721 (1992).

[7] A. Ennaoui, S. Fiechter, H. Tributsch, M. Giersig, R. Vogel, and H. Weller, Photoelectrochemical energy conversion obtained with ultrathin organo-metallic-chemical-vapor-deposition layer of FeS_2 (pyrite) on TiO_2, J. Electrochem. Soc. **139**, 2514 (1992).

[8] M. Bronold, K. Büker, S. Kubala, C. Pettenkofer, and H. Tributsch, Surface preparation of FeS_2 via electrochemical etching and interface formation with metals, Phys. Status Solidi **135**, 231 (1993).

[9] M. Bronold, Y. Tomm, and W. Jaegermann, Surface states on cubic d-band semiconductor pyrite (FeS_2), Surf. Sci. **314**, L931 (1994).

[10] Y. Bi, Y. Yuan, C. L. Exstrom, S. A. Darveau, and J. Huang, Air stable, photosensitive, phase pure iron pyrite nanocrystal thin films for photovoltaic application, Nano Lett. **11**, 4953 (2011).

[11] M. Cabán-Acevedo, M. S. Faber, Y. Tan, R. J. Hamers, and S. Jin, Synthesis and properties of semiconducting iron pyrite (FeS_2) nanowires, Nano Lett. **12**, 1977 (2012).

[12] C. Steinhagen, T. B. Harvey, C. J. Stolle, J. Harris, and B. A. Korgel, Pyrite nanocrystal solar cells: Promising, or fool's gold? J. Phys. Chem. Lett. **3**, 2352 (2012).

[13] M. Cabán-Acevedo, D. Liang, K. S. Chew, J. P. DeGrave, N. S. Kaiser, and S. Jin, Synthesis, characterization, and variable range hopping transport of pyrite (FeS_2) nanorods, nanobelts, and nanoplates, ACS Nano **7**, 1731 (2013).

[14] M. Cabán-Acevedo, N. S. Kaiser, C. R. English, D. Liang, B. J. Thompson, H. Chen, K. J. Czech, J. C. Wright, R. J. Hamers, and S. Jin, Ionization of high-density deep donor defect states explains the low photovoltage of iron pyrite single crystals, J. Am. Chem. Soc. **136**, 17163 (2014).

[15] S. Shukla, G. Xing, H. Ge, R. R. Prabhakar, S. Mathew, Z. Su, V. Nalla, T. Venkatesan, N. Mathews, T. Sritharan, T. C. Sum, and Q. Xiong, Origin of photocarrier losses in iron pyrite (FeS_2) nanocubes, ACS Nano **10**, 4431 (2016).

[16] R. Sun, M. K. Y. Chan, and G. Ceder, First-principles electronic structure and relative stability of pyrite and marcasite: Implications for photovoltaic performance, Phys. Rev. B **83**, 235311 (2011).

[17] L. Yu, S. Lany, R. Kykyneshi, V. Jieratum, R. Ravichandran, B. Pelatt, E. Altschul, H. A. S. Platt, J. F. Wager, D. A. Keszler, and A. Zunger, Iron chalcogenide photovoltaic absorbers, Adv. Energy Mater. **1**, 748 (2011).

[18] N. Berry, M. Cheng, C. L. Perkins, M. Limpinsel, J. C. Hemminger, and M. Law, Atmospheric-pressure chemical vapor deposition of iron pyrite thin films, Adv. Energy Mater. **2**, 1124 (2012).

[19] S. Seefeld, M. Limpinsel, Y. Liu, N. Farhi, A. Weber, Y. Zhang, N. Berry, Y. J. Kwon, C. L. Perkins, J. C. Hemminger, R. Wu, and M. Law, Iron pyrite thin films synthesized from an ink, J. Am. Chem. Soc. **135**, 4412 (2013).

[20] X. Zhang, T. Scott, T. Socha, D. Nielsen, M. Manno, M. Johnson, Y. Yan, Y. Losovyj, P. Dowben, E. S. Aydil, and C. Leighton, Phase stability and stoichiometry in thin film iron pyrite: Impact on electronic transport properties, ACS Appl. Mater. Interfaces **7**, 14130 (2015).

[21] J. Puthussery, S. Seefeld, N. Berry, M. Gibbs, and M. Law, Colloidal iron pyrite (FeS_2) nanocrystal inks for thin-film photovoltaics, J. Am. Chem. Soc. **133**, 716 (2011).

[22] J. M. Lucas, C. Tuan, S. D. Lounis, D. K. Britt, R. Qiao, W. Yang, A. Lanzara, and A. P. Alivisatos, Ligand-controlled colloidal synthesis and electronic structure characterization of cubic iron pyrite (FeS_2) nanocrystals, Chem. Mater. **25**, 1615 (2013).

[23] X. Zhang, M. Manno, A. Baruth, M. Johnson, E. S. Aydil, and C. Leighton, Crossover From nanoscopic intergranular hopping to conventional charge transport in pyrite thin films, ACS Nano **7**, 2781 (2013).

[24] R. J. Soukup, P. Prabukanthan, N. J. Ianno, A. Sarkar, C. A. Kamler, and D. G. Sekora, Formation of pyrite (FeS_2) thin films by thermal sulfurization of dc magnetron sputtered iron, J. Vac. Sci. Technol. A **29**, 011001 (2011).

[25] X. Zhang, M. Li, J. Walter, L. O'Brien, M. A. Manno, B. Voigt, F. Mork, S. V. Baryshev, J. Kakalios, E. S. Aydil, and C. Leighton, Potential resolution to the doping puzzle in iron pyrite: Carrier type determination by Hall effect and thermopower, Phys. Rev. Mater. **1**, 15402 (2017).

[26] T. Kinner, K. P. Bhandari, E. Bastola, B. M. Monahan, N. O. Haugen, P. J. Roland, T. P. Bigioni, and R. J. Ellingson, Majority carrier type control of cobalt iron sulfide ($Co_xFe_{1-x}S_2$) pyrite nanocrystals, J. Phys. Chem. C **120**, 5706 (2016).

[27] M. Limpinsel, N. Farhi, N. Berry, J. Lindemuth, C. L. Perkins, Q. Lin, and M. Law, An inversion layer at the surface of n-type iron pyrite, Energy Environ. Sci. **7**, 1974 (2014).

[28] R. Morrish, R. Silverstein, and C. A. Wolden, Synthesis of stoichiometric FeS_2 through plasma-assisted sulfurization of nanorods, J. Am. Chem. Soc. **134**, 17854 (2012).

[29] L. Friedman, Hall conductivity of amorphous semiconductors in the random phase model, J. Non Cryst. Solids **6**, 329 (1971).

[30] P. G. Le Comber, D. I. Jones, and W. E. Spear, Hall effect and impurity conduction in substitutionally doped amorphous silicon, Philos. Mag. **35**, 1173 (1977).

[31] Yu. M. Gal'perin, E. P. German, and V. G. Karpov, Hall effect under hopping conduction conditions, Zh. Eksp. Teor. Fiz. **99**, 343 (1991) [Sov. Phys. JETP **72**, 193 (1991)].

[32] J. Kakalios, A physical interpretation of the Hall effect in amorphous semiconductors, J. Non Cryst. Solids **114**, 372 (1989).

[33] I. P. Zvyagin, On the theory of hopping transport in disordered semiconductors, Phys. Status Solidi **58**, 443 (1973).

[34] H. Overhof, Thermopower calculation for variable range hopping—Application to α-Si, Phys. Status Solidi **67**, 709 (1975).

[35] A. J. Lewis, Conductivity and thermoelectric power of amorphous germanium and amorphous silicon, Phys. Rev. B **13**, 2565 (1976).

[36] S. Shukla, N. H. Loc, P. P. Boix, T. M. Koh, R. R. Prabhakar, H. K. Mulmudi, J. Zhang, S. Chen, C. F. Ng, C. H. A. Huan, N. Mathews, T. Sritharan, and Q. Xiong, Iron pyrite thin film counter electrodes for dye-sensitized solar cells: High efficiency for iodine and cobalt redox electrolyte cells, ACS Nano **8**, 10597 (2014).

[37] A. Yamamoto, M. Nakamura, A. Seki, E. L. Li, A. Hashimoto, and S. Nakamura, Pyrite (FeS_2) thin films prepared by spray method, Sol. Energy Mater. Sol. Cells **75**, 451 (2003).

[38] D. Lichtenberger, K. Ellmer, R. Schieck, S. Fiechter, and H. Tributsch, Structural, optical and electrical properties of polycrystalline iron pyrite layers deposited by reactive d.c. magnetron sputtering, Thin Solid Films **246**, 6 (1994).

[39] G. Willeke, R. Dasbach, B. Sailer, and E. Bucher, Thin pyrite (FeS_2) films prepared by magnetron sputtering, Thin Solid Films **213**, 271 (1992).

[40] F. W. Herbert, A. Krishnamoorthy, K. J. Van Vliet, and B. Yildiz, Quantification of electronic band gap and surface states on FeS_2 (100), Surf. Sci. **618**, 53 (2013).

[41] Y. N. Zhang, J. Hu, M. Law, and R. Q. Wu, Effect of surface stoichiometry on the band gap of the pyrite FeS_2 (100) surface, Phys. Rev. B **85**, 085314 (2012).

[42] D. R. Alfonso, Computational investigation of FeS_2 surfaces and prediction of effects of sulfur environment on stabilities, J. Phys. Chem. C **114**, 8971 (2010).

[43] J. Hu, Y. Zhang, M. Law, and R. Wu, First-principles studies of the electronic properties of native and substitutional anionic defects in bulk iron pyrite, Phys. Rev. B **85**, 085203 (2012).

[44] P. Lazić, R. Armiento, F. W. Herbert, R. Chakraborty, R. Sun, M. K. Y. Chan, K. Hartman, T. Buonassisi, B. Yildiz, and G. Ceder, Low intensity conduction states in FeS_2: Implications for absorption, open-circuit voltage and surface recombination, J. Phys. Condens. Matter **25**, 465801 (2013).

[45] T. Thio and J. W. Bennett, Hall effect and conductivity in pyrite NiS_2, Phys. Rev. B **50**, 10574 (1994).

[46] T. Thio, J. W. Bennett, and T. R. Thurston, Surface and bulk magnetic properties of pyrite NiS_2: Magnetization and neutron-scattering studies, Phys. Rev. B **52**, 3555 (1995).

[47] N. Wu, R. F. Sabirianov, W. N. Mei, Y. B. Losovyj, N. Lozova, M. Manno, C. Leighton, and P. A. Dowben, The minority spin surface bands of CoS_2 (001), J. Phys. Condens. Matter **21**, 295501 (2009).

[48] M. Z. Hasan and C. L. Kane, Colloquium: Topological insulators, Rev. Mod. Phys. **82**, 3045 (2010).

[49] X.-L. Qi and S.-C. Zhang, Topological insulators and superconductors, Rev. Mod. Phys. **83**, 1057 (2011).

[50] D. J. Kim, J. Xia, and Z. Fisk, Topological surface state in the Kondo insulator samarium hexaboride, Nat. Mater. **13**, 466 (2014).

[51] S. Wolgast, Ç. Kurdak, K. Sun, J. W. Allen, D.-J. Kim, and Z. Fisk, Low-temperature surface conduction in the Kondo insulator SmB_6, Phys. Rev. B **88**, 180405 (2013).

[52] J. A. Maxwell, J. L. Campbell, and W. J. Teesdale, The Guelph PIXE software package, Nucl. Instrum. Methods Phys. Res. B **43**, 218 (1989).

[53] L. J. van der Pauw, A method of measuring the resistivity and Hall coefficient on lamellae of arbitrary shape, Philips Tech. Rev. **20**, 220 (1958).

[54] T. P. Mernagh and A. G. Trudu, A laser Raman microprobe study of some geologically important sulphide minerals, Chem. Geol. **103**, 113 (1993).

[55] https://www.alfa.com/en/catalog/012842/

[56] H. C. Montgomery, Method for measuring electrical resistivity of anisotropic materials, J. Appl. Phys. **42**, 2971 (1971).
[57] See Supplemental Material at http://link.aps.org/supplemental/10.1103/PhysRevMaterials.1.065403 for additional information on the thickness dependence of resistivity and the derivation of $R_H(B_\perp)$.
[58] N. F. Mott, *Metal-Insulator Transitions*, 2nd ed. (CRC, London, 1990).
[59] B. I. Shklovskii and A. L. Efros, *Electronic Properties of Doped Semiconductors*, Springer Series in Solid-State Sciences (Springer, Berlin, 1984).
[60] R. C. O'Handley, *Modern Magnetic Materials - Principles and Applications* (Wiley, New York, 2000).
[61] P. A. Lee and T. V. Ramakrishnan, Disordered electronic systems, Rev. Mod. Phys. **57**, 287 (1985).
[62] G. Bergmann, Weak localization in thin films—A time-of-flight experiment with conduction electronics, Phys. Rep. **107**, 1 (1984).
[63] We refer here to weakly localized transport in 2D as effectively metallic. For a fuller discussion see Refs. [64] and [65].
[64] W. Xie, X. Zhang, C. Leighton, and C. D. Frisbie, 2D insulator-metal transition in aerosol-jet-printed electrolyte-gated indium oxide thin film transistors, Adv. Electron. Mater. **3**, 1600369 (2017).
[65] S. Das Sarma and E. H. Hwang, Two-dimensional metal-insulator transition as a strong localization induced crossover phenomenon, Phys. Rev. B **89**, 235423 (2014).
[66] We are again here treating this system as effectively a 2D metal. Use of the Thouless length as opposed to the mean-free path would produce a less stringent estimate for t_s.
[67] A. G. Zabrodskii, The Coulomb gap: The view of an experimenter, Philos. Mag. B **81**, 1131 (2001).
[68] M. Law (private communication).
[69] S. M. Sze, *Physics of Semiconductor Devices* (John Wiley & Sons, New York, 1981).
[70] E. Conwell and V. F. Weisskopf, Theory of impurity scattering in semiconductors, Phys. Rev. **77**, 388 (1950).
[71] H. Brooks, Scattering by ionized impurities in semiconductors, Phys. Rev. **83**, 879 (1951).
[72] R. Schieck, A. Hartmann, S. Fiechter, R. Konenkamp, and H. Wetzel, Electrical properties of natural and synthetic pyrite (FeS_2) crystals, J. Mater. Res. **5**, 1567 (1990).
[73] R. Murphy and D. Strongin, Surface reactivity of pyrite and related sulfides, Surf. Sci. Rep. **64**, 1 (2009).
[74] H. W. Nesbitt, G. M. Bancroft, A. R. Pratt, and M. J. Scaini, Sulfur and iron surface states on fractured pyrite surfaces, Am. Mineral. **83**, 1067 (1998).
[75] K. Andersson, M. Nyberg, H. Ogasawara, D. Nordlund, T. Kendelewicz, C. S. Doyle, G. E. Brown, L. G. M. Pettersson, and A. Nilsson, Experimental and theoretical characterization of the structure of defects at the pyrite FeS_2 (100), Phys. Rev. B **70**, 195404 (2004).
[76] R. Sun, M. K. Y. Chan, S. Y. Kang, and G. Ceder, Intrinsic stoichiometry and oxygen-induced p-type conductivity of pyrite FeS_2, Phys. Rev. B **84**, 035212 (2011).
[77] Q. Hu, D. Y. Kim, W. Yang, L. Yang, Y. Meng, L. Zhang, and H.-K. Mao, FeO_2 and FeOOH under deep lower-mantle conditions and Earth's oxygen–hydrogen cycles, Nature (London) **534**, 241 (2016).
[78] S. S. Streltsov, A. O. Shorikov, S. L. Skornyakov, A. I. Poteryaev, and D. I. Khomskii, Unexpected 3+ valence of iron in FeO_2, a geologically important material lying "in between" oxides and peroxides, Sci. Rep. **7**, 13005 (2017).